Journal of Volcanology and Geothermal Research 447 (2024) 108027

Contents lists available at ScienceDirect

Journal of Volcanology and Geothermal Research

journal homepage: www.journals.elsevier.com/journal-of-volcanology-and-geothermal-research

The 2021 eruption of Pacaya Volcano, Guatemala – Geophysical analysis through satellite geodesy and seismic noise correlations

J. Gonzalez-Santana [a], C. Wauthier [a,b,*], G. Waite [c]

[a] Department of Geosciences, The Pennsylvania State University, Deike Building, University Park 16802, PA, USA
[b] Institute for Computational and Data Sciences, The Pennsylvania State University, University Park 16802, PA, USA
[c] Department of Geological and Mining Engineering and Sciences, Michigan Technological University, Houghton 49931, MI, USA

ARTICLE INFO

Original content: Lava flow and vent shapefiles for: The 2021 eruption of Pacaya Volcano, Guatemala – geophysical analysis through satellite geodesy and seismic noise correlations (Original data)

Keywords:
InSAR
Time-series analysis
Seismic cross-correlation
Seismic auto-correlation
Pacaya Volcano

ABSTRACT

Pacaya is an active basaltic volcano in Guatemala, that underwent a heightened period of volcanic activity in early 2021, as the culmination of effusive and explosive activity starting in mid-2015. We present an assessment of the geophysical signals associated with this heightened eruptive interval leveraging access to ground deformation data from 9 Synthetic Aperture Radar (SAR) datasets acquired by 5 different radar satellite platforms and seismic data from 4 permanent stations. Given evidence for past vigorous eruptive activity from vents beyond the summit area being associated with initiated or accelerated flank creep, we assess whether this process occurred also in 2021 or not. Further, the availability of a dense SAR dataset with different spatial and temporal resolutions is leveraged as an incomparable opportunity to assess the relative performance of different SAR platforms for monitoring volcanic eruptions. The more limited seismic dataset is used for comparison of peaks in real-time seismic amplitude measurement (RSAM) time-series, as well as velocity variations derived from single-station cross-component correlations (SC) and auto-correlations (AC), with changes in volcanic activity. The SAR time-series results reveal displacements compatible with down-dip motion of the unstable southwest flank (downward vertical and westward horizontal displacements), but there might be contributions to the signal from lava flow compaction and seasonal tropospheric water vapor variations. RSAM peaks appear to reflect vigor of lava effusion at Pacaya but gaps in the data impede the assessment of whether there were recognizable signals during times of change in eruptive behavior. Single-station correlations captured the effects of rainfall variability but were otherwise too noisy to draw clear insights. Overall, this study showcases the challenges of coherence loss during periods with widespread lava effusion and ash fall, and the advantages of performing time-series analysis on shorter subsets of time to retain more pixels in times of lower volcanic activity. Additionally, our results highlight the advantage of high spatial resolution SAR amplitude imagery for mapping surface changes, the vulnerability to geometric distortions of low incidence angle platforms, and the challenge of relying on tasking to obtain timely satellite imagery over active volcanoes.

1. Introduction

Pacaya is an active basaltic stratovolcano in Guatemala, which experienced flank collapse between 0.6 and 1.6 ka, producing a 0.65 km^3 debris avalanche that traveled >25 km away from the cone (Kitamura and Matías, 1995; Rose et al., 2013; Siebert et al., 2006; Vallance et al., 1995). Recent radar satellite geodesy (Interferometric Synthetic Aperture Radar, InSAR) studies at Pacaya identified transient flank instability events during large eruptions in 2010 and 2014 that persisted at a decaying rate for 2–3 years after each eruption (Schaefer et al., 2015, 2017; Wnuk and Wauthier, 2017; Gonzalez-Santana and Wauthier, 2021; Gonzalez-Santana et al., 2022). Fig. 1 shows a timeline of the slip rates obtained from these InSAR studies along the top, and a description of the concurrent eruptive activity styles along the bottom. Slip rates were obtained from the same time-series location on the southwest flank of Pacaya (Gonzalez-Santana et al., 2022). The initiation and acceleration of flank creep during the eruptions in 2010 and 2014, in orange, coincided with the opening of NNW–SSE oriented vents away from the main open conduit. This was in contrast to other times of lava effusion and explosive activity from 2006 to 2010 and 2018 to 2020, in purple, where flank displacements were negligible. Therefore, the opening of vents beyond the summit was proposed to indicate heightened

* Corresponding author at: Department of Geosciences, The Pennsylvania State University, Deike Building, University Park 16802, PA, USA.
E-mail address: cuw25@psu.edu (C. Wauthier).

https://doi.org/10.1016/j.jvolgeores.2024.108027
Received 30 August 2023; Received in revised form 30 January 2024; Accepted 3 February 2024
Available online 7 February 2024

likelihood of renewed or increased flank creep (Gonzalez-Santana et al., 2022).

A heightened eruptive period took place at Pacaya from December 2020 to May 2021 (Fig. 1). The aims of this study were to identify potential structural changes in the edifice over time during the eruptive interval using Synthetic Aperture Radar (SAR) amplitude imagery, to characterize any further flank deformation events using InSAR ground deformation maps and time-series, and to update the lava flow maps using optical and thermal satellite imagery. In particular, InSAR time-series analysis allows investigation into whether this eruption was accompanied by accelerated flank creep, as expected based on the conceptual model presented by Gonzalez-Santana et al. (2022). Given the association between prior opening of vents beyond the summit area and renewed or increased flank creep, we produced maps of lava flows and tracked vent locations using thermal imagery and false-color composites of multi-spectral data, to compare the timing of these changes in flank displacements with likely changes in magma ascent pathways.

Four seismic stations were intermittently active between the end of 2019 and the end of 2022 at Pacaya (Fig. 2), motivating a secondary aim to compare both geophysical datasets, in a search for further insights into the underlying processes operating at Pacaya during large eruptions. Specifically, we leverage Real-time Seismic Amplitude Measurements (RSAM) and single-station seismic ambient noise cross-correlations. At Pacaya, INSIVUMEH reports suggest a close relation between explosive vigor and RSAM values, thus we compile RSAM time-series to track the state of activity during the eruptive crisis. Temporal perturbations in cross-correlated seismic ambient noise fields between two stations, or components of a single station, can be used to produce time-series of seismic velocity changes (Brenguier et al., 2008; De Plaen et al., 2016; Donaldson et al., 2017). These changes have been used to detect pre-eruptive seismic velocity drops as well as track climate-related changes (De Plaen et al., 2016), thus we compile single-station seismic ambient noise cross-correlations to track velocity changes before, during, and after the eruptive crisis.

A call for international assistance during this eruptive crisis resulted in the tasking of satellites to collect additional and higher spatial resolution SAR data than that usually available over Pacaya from missions with regular orbits and acquisitions. This resulted in access to SAR data from a total of 5 satellite platforms, 4 of which had data in both ascending (satellite flying south to north) and descending (satellite flying north to south) orbits, yielding 9 individual datasets spanning either the entirety, the second half, or the end of the eruptive crisis. In addition to the scientific aims presented above, the availability of such a dataset composed of X-band (~3.1 cm wavelength), C-band (~5.5 cm wavelength), and L-band (~23.6 cm wavelength) data with different spatial and temporal resolutions and incidence angles provided an incomparable opportunity to assess the relative performance of different SAR platforms for monitoring volcanic eruptions. Thus, we present a case study of the strengths and weaknesses of each of these datasets in the context of monitoring active volcanic eruptions and surface changes.

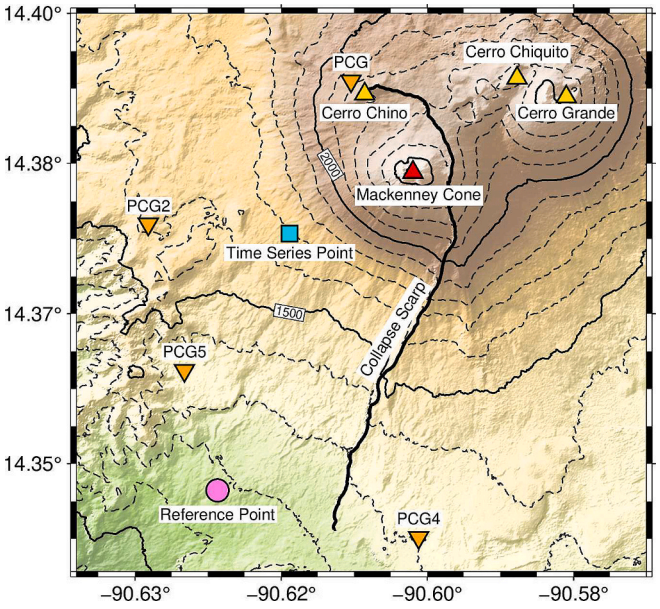

Fig. 2. Map of Pacaya volcano showing the outline of the ancestral collapse scarp in black, the locations of the main active cone, the Mackenney Cone (red triangle), and old domes Cerro Grande, Cerro Chiquito and Cerro Chino (yellow triangles). The orange inverted triangles show the location of seismic stations (PCG, PCG2, PCG4, PCG5), and the pink circle and blue square respectively show the reference point and time-series point used for InSAR time-series processing. (For interpretation of the references to color in this figure legend, the reader is referred to the web version of this article.)

1.1. The 2021 eruption sequence

The eruptive period leading to the 2021 crisis began in June 2015 with incandescence and intermittent ash venting, following Strombolian explosions and effusive activity in January and March 2014 and intermittent ash venting through February 2015 (Global Volcanism Program, 2013; Wnuk and Wauthier, 2017; Gonzalez-Santana et al., 2022). The amount of incandescence increased throughout 2015, and Strombolian activity built an intra-crater cone in 2016, filling most of the crater by 2017 (Global Volcanism Program, 2013). New lava flows erupted from the summit area on January–April 2017 and explosions persisted through 2017. Strombolian activity and lava effusion continued in 2019

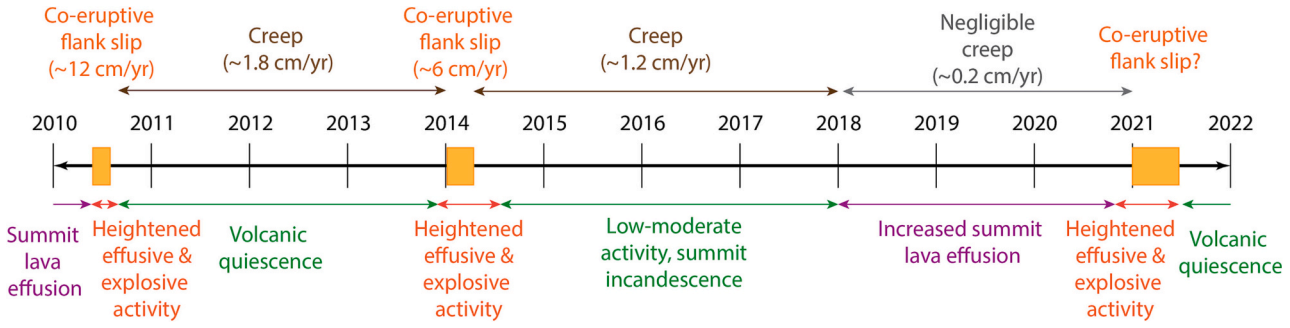

Fig. 1. Timeline of the main activity styles at Pacaya volcano between 2010 and 2022. The flank slip rate estimates along the top are from the InSAR time-series of Gonzalez-Santana et al. (2022). Co-eruptive slip is shown in orange, slower decaying slip rates after the eruptions in brown, and negligible displacements in grey. The activity descriptions along the bottom were condensed from Global Volcanism Program Reports, INSIVUMEH bulletin reports, thermal anomaly time-series, and the lava flow map observations presented in Gonzalez-Santana et al. (2022). Orange descriptions correspond to heightened activity involving lava effusion from vents beyond the summit, purple descriptions correspond to times of lava effusion from the summit, and green descriptions represent times of low volcanic activity. (For interpretation of the references to color in this figure legend, the reader is referred to the web version of this article.)

and 2020, with increased explosive activity and effusion from August–December 2020 (Global Volcanism Program, 2013; Gonzalez-Santana et al., 2022).

On October 20, 2020, a new lava flow erupted from vents lower on the west flank of Pacaya, in contrast to earlier flows in 2019–2020, that had mostly initiated near the summit crater. Increased explosive and effusive activity was registered starting on December 2020, with flows extending >1 km (Global Volcanism Program, 2013). Explosivity increased again in February 2021 through mid-May, with a further increase in activity in March relative to the already elevated activity levels in February. Ash plumes throughout March 2021 reached up to 5.4 km above sea-level, and on March 23 led to the closure of the La Aurora International Airport in Guatemala City, ~25 km away. Multiple flows initiated on the south, southeast, and southwest flanks through March. There was a reduction in ash venting after April 9, but new flows initiated on April 27–29. May 17 marked the end of effusive activity for this eruption, from the final fissure that opened on April 29. The last recorded ash fall for this eruptive interval was on May 26, prior to a return to ash venting at background levels (Global Volcanism Program, 2013).

2. Methods

To provide a detailed overview of the events associated with the early 2021 eruptive crisis at Pacaya, we compiled lava flow maps, radar satellite geodesy (SAR) data, and seismic data. The following sections introduce each of these datasets.

2.1. Lava Flow Maps

Optical imagery was used to track the evolution of lava effusion at Pacaya. Level 2 Landsat 7 and 8 data were obtained from EarthExplorer (https://earthexplorer.usgs.gov/) and Glovis (https://glovis.usgs.gov/app), and Sentinel-2 Full Resolution Browse GeoTIFF granules were obtained from EarthExplorer. We downloaded 21 Landsat-8 tiles between August 1, 2020, and June 17, 2021, and 20 Landsat-7 tiles from August 9, 2020, to June 9, 2021, both acquired every 16 days, and 63 Sentinel-2 tiles between August 7, 2020, and June 13, 2021, acquired every 5 days.

To better visualize the thermal anomalies from lava flows and crater incandescence, we produced Red-Green-Blue false image band combinations using the short-wave infrared (SWIR), near-infrared (NIR), and red bands for each of the optical datasets, in QGIS (https://www.qgis.org/en/site/). These correspond to bands 7, 5, and 4 for Landsat-8, bands 7, 4, and 3 for Landsat-7, and bands 12, 8a, and 4 for Sentinel-2. The Landsat bands have a spatial resolution of 30 m, whereas Sentinel-2 data have a spatial resolution of 20 m for bands 12 and 8a, and 10 m for band 4.

We inspected all images for the presence of visible thermal anomalies, regardless of cloud cover, and generated shapefiles for lava flows or portions of lava flows that were not covered by clouds. We also identified the approximate location of effusive vents by selecting the topographically highest point on thermal anomalies. Lava flows and vents were then manually grouped into subsets, or epochs, sharing similar source locations to highlight changes in lava effusion behavior throughout the study period. Finally, we outlined the extent of lava flows for each of the identified epochs to obtain the area covered by lava during each epoch and estimated the erupted volume using an average lava flow thickness of 2 m (Matías Gomez et al., 2012; Wnuk and Wauthier, 2017) (see Supporting Information, section S1).

2.2. Radar satellite data

We compiled a total of 9 SAR datasets from 5 different satellite platforms, with acquisitions in both ascending and descending orbits for 4 of the platforms, starting before, during, and directly after the 2021 eruptive crisis. While describing the events of the 2021 crisis, we refer to the 'pre-crisis interval' as any dates prior to October 20, 2020, when vents first opened away from the main summit region. The 'co-eruptive interval' spans October 20, 2020 to May 26, 2021, the date of the last ash venting event associated with the eruption, and the 'post-eruptive interval' captures all available data beyond May 26, 2021. Fig. 3 shows the times spanned by each of the datasets presented in this study relative to the crisis start and end (red and black dashed vertical lines, respectively), and Table 1 provides extra details on all 9 datasets. Sentinel-1, COSMO-SkyMed, and ALOS-2 data covered the full study period, whereas TerraSAR-X tasking only began during the height of the eruptive crisis and RADARSAT-2 data were only available starting after the eruption.

ALOS-2 is an L-band SAR satellite from the Japan Aerospace Exploration Agency (JAXA) that was launched in 2014. Level 1.1 Single Look Complex (SLC) images for path 148, row 3300, were downloaded through the JAXA G-Portal and EORC Order Desk. These ScanSAR imaging mode scenes have a spatial resolution of 100 m, covering 350 km wide swaths. Repeat acquisitions over Pacaya were not available on regular intervals, with only 8 descending scenes available between 2020–01–01 and 2022–09–01. The shortest repeat interval is just under 3 months and the longest just over 6 months.

Sentinel-1 is a C-band SAR satellite constellation from the European Space Agency (ESA) launched between 2014 and 2016. This constellation had a repeat cycle of 6 days through December 2021. Level 1 SLC data were downloaded through the Alaska Satellite Facility Vertex portal (https://search.asf.alaska.edu) and corresponding precise orbit files were obtained from the ESA's Copernicus Sentinels Precise Orbit Determination Data Hub. These data were acquired in the Interferometric Wide (IW) swath mode, composed of 250 km wide swaths with a spatial resolution of 5 m in range (along the satellite viewing angle, perpendicular to the flight direction) and of 20 m in azimuth (parallel to the satellite flight direction). This mode acquires data across 3 swaths (IW1–IW3), with several bursts (typically 6–9) in each swath, that can be processed as separate SLC images, or stitched together. For the case of Pacaya, only one burst from swath IW2 on path 26 was required in the descending orbit, whereas 2 bursts were processed from swath IW2 on path 136 to guarantee full coverage in the ascending orbit.

COSMO-SkyMed is a constellation of 4 X-band SAR satellites from the Italian Space Agency (ASI), launched between 2007 and 2010. Level 1A SLC data were provided by ASI through the Committee on Earth Observation Satellites (CEOS) Volcano Demonstrator. These Stripmap Himage imaging mode scenes have a spatial resolution of 3 m and 40 km wide swaths. Images over Pacaya were available every ~8 and ~16 days in the ascending and descending orbits, respectively.

TerraSAR-X is an X-band SAR satellite from the German Space Agency (DLR), that was launched in June 2007. Level 1B SLC data were downloaded through the CEOS-hosted Supersites repository. These Spotlight imaging mode scenes have a spatial resolution of 1.2 m in range and of 1.7 m in azimuth, 10 km wide swaths, and a repeat acquisition interval of 11 days.

RADARSAT-2 is a C-band SAR satellite from the Canadian Space Agency (CSA), launched in December 2007. SLC data were provided through the Volcano Disasters Assistance Program (VDAP), courtesy of the National Geospatial Intelligence Agency and the U.S. Geological Survey. These Spotlight imaging mode scenes have a spatial resolution of 1 m and 20 km wide swaths, with a repeat acquisition interval of 24 days.

SAR images are complex and thus can be decomposed into 1) the amplitude, a measure of backscattered radar signal reflectivity that depends on the backscattering properties of the ground (mostly roughness and electrical conductivity), the radar wavelength, and the local incidence angle, and 2) the phase, which is a function of the distance between the sensor and the ground and the radar wavelength. Interferometric Synthetic Aperture Radar (InSAR) uses the difference in phase between two SAR images to produce a map of surface deformation

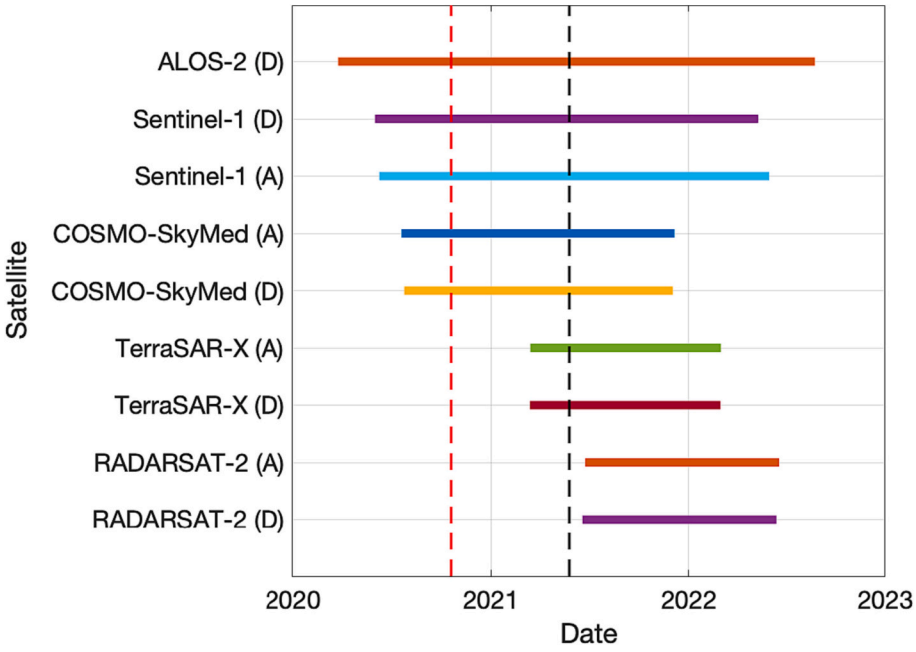

Fig. 3. Time-span of the SAR data used in this study. The vertical red dashed line marks the timing of first vent opening beyond the summit crater on October 10, 2020, and the dashed black line marks the timing of the final ash venting recorded on May 26, 2021. D = descending orbit; A = ascending orbit. (For interpretation of the references to color in this figure legend, the reader is referred to the web version of this article.)

Table 1
SAR data information and processing parameters. D = descending; A = ascending; Igms = interferograms; Pol = polarization; ML = multi-looks: range, azimuth; Inc. = incidence angle (degrees), λ = wavelength (cm); $B_\perp$ = perpendicular baseline (m); B_T = temporal baseline (days).

Dataset	Orbit	Start Date	End Date	# Scenes	# Igms	Pol	ML	Inc	λ	$B_\perp$	B_T
ALOS-2	D	2020-03-25	2022-08-24	8	16	HH	2, 9	39	24.2	600	365
Sentinel-1	D	2020-06-01	2022-05-10	107	315	VV	8, 2	39	5.5	Daisies	
Sentinel-1	A	2020-06-09	2022-05-30	107	314	VV	8, 2	39	5.5	Daisies	
COSMO-SkyMed	A	2020-07-20	2021-12-06	58	341	HH	6, 8	24	3.1	500	150
COSMO-SkyMed	D	2020-07-25	2021-12-03	15	24	HH	6, 6	27	3.1	500	150
TerraSAR-X	A	2021-03-15	2022-03-02	25	65	HH	5, 5	23	3.1	350	60
TerraSAR-X	D	2021-03-14	2022-03-01	24	71	HH	5, 5	22	3.1	350	60
RADARSAT-2	A	2021-06-24	2022-06-19	15	65	HH	4, 14	38	5.5	200	200
RADARSAT-2	D	2021-06-19	2022-06-14	16	89	HH	4, 14	44	5.5	200	200

in the Line Of Sight (LOS) of the satellite (Massonnet and Feigl, 1998; Simons and Rosen, 2015). The interferometric process produces wrapped interferograms, which show fringes, or full color cycles, corresponding to phase changes between 0 and 2π, or half the wavelength of the satellite. Wavelengths for each satellite are included in Table 1. This observed relative phase signal is the modulo-2π of the unknown absolute phase signal or total deformation (Massonnet and Feigl, 1998; Hanssen, 2001; Simons and Rosen, 2015). An interferogram showing this modulo-2π ambiguity is termed "wrapped", and the process whereby this ambiguity is resolved is called "unwrapping".

SAR data from all platforms were processed using the GAMMA software (Werner et al., 2001). SAR scenes for each dataset were co-registered and geocoded using a 12 m TanDEM-X Digital Elevation Model (DEM). Multi-looking, or spatial averaging, was performed using the range (perpendicular to flight direction) and azimuth (parallel to flight direction) multi-look values listed in Table 1. First, we inspected the multi-looked, geocoded, amplitude products to identify any changes in scattering properties of the edifice resulting from lava flow effusion, ash fall, or cone collapses during the eruption. We then produced interferograms for each dataset, by combining pairs of scenes with small enough perpendicular (perpendicular distance between the satellite positions) and temporal (time between acquisitions) baselines. For Sentinel-1, given the relatively small baselines and short repeat acquisition periods, we created pairs for each date with the consecutive 3 dates using a "daisy-chain" approach (e.g., Ebmeier, 2016). For all other datasets we set temporal and perpendicular baseline thresholds based on maximizing the number of pairs creating a well-connected network (at least 2 interferograms per scene) while retaining coherence for the final products. Coherence, with values between 0 and 1, quantifies the degree to which the scattering properties remain stable between the two scenes, where a decrease in coherence corresponds to decorrelation of the interferometric signal. Decorrelation arises when the phase changes by 2π or more within a range resolution element (Hanssen, 2001; Pinel et al., 2014). The chosen baseline thresholds are listed in Table 1. Fig. S8 shows a plot of the interferogram networks used for time-series analysis of all datasets. Consecutive interferograms were also created between each date and the next, regardless of perpendicular baseline, as inputs for stacking to enhance signal-to-noise ratios. All interferograms were filtered using a 0.4 strength adaptive spectral filter (Goldstein and Werner, 1998) and unwrapped, which resolves the observed relative phase signal from the wrapped interferogram into an absolute phase signal, using the Minimum Cost Flow algorithm (Costantini, 1998) with an irregular triangular network (Costantini and Rosen, 1999). Finally, the unwrapped phase was converted to displacement.

InSAR time-series analysis was performed using the Small BAselines

Subset (SBAS) method (Berardino et al., 2002; Lundgren et al., 2001), implemented in the MSBASv3 software (Samsonov, 2019). This technique extracts the satellite LOS displacements over time through pixel-by-pixel linear least squares inversion of the mean phase velocity between each time interval between dates, using the first date as reference (Berardino et al., 2002), and can increase the signal-to-noise ratio of InSAR datasets and thus extract smaller magnitude signals. In fact, previous work showed that for Sentinel-1 time-series over Pacaya, the predicted ~10 cm annual amplitude of signal variation resulting from seasonal changes in tropospheric water vapor content was reduced to ~2.5 cm when applying SBAS time-series analysis (Gonzalez-Santana et al., 2022).

Since SBAS calculates the time-series on a pixel-by-pixel basis for pixels which are coherent in all input interferograms, final products can be sparse if datasets span periods of significant surface property changes, such as lava effusion and ash fall, as was the case during the 2021 eruptive crisis. In order to mitigate some of the loss of coherence, which manifests as no-data regions in SBAS results, we also calculated time-series for subsets of data spanning the pre-crisis (prior to October 20, 2020), co-eruptive (October 20, 2020 – May 26, 2021), and post-eruptive (after May 26, 2021) intervals, for datasets where enough scenes were available. TerraSAR-X data only spanned the co-eruptive and post-eruptive periods, and RADARSAT-2 only spanned the post-eruptive period. Additionally, there were too few descending COSMO-SkyMed acquisitions to produce pre-crisis and post-eruptive time-series, and too few ALOS-2 acquisitions to calculate any subsets.

Given the availability of overlapping datasets with different look angles, we applied an extension to the SBAS approach, the multidimensional SBAS (MSBAS), also implemented through the MSBASv3 software (Samsonov, 2019), to calculate a joint time-series with all 9 datasets. This technique leverages the availability of different viewing geometries from two or more datasets to extract the horizontal and vertical displacement components, in place of the LOS displacements (Samsonov and D'Oreye, 2012, 2017). All SBAS and MSBAS time-series processing used a reference region at the foot of the southwest flank of Pacaya that remained coherent in all SAR datasets (Fig. 2).

Finally, to assess the improvement in performance of time-series derived maps over conventional InSAR interferograms, we produced long interval interferograms for the pre-crisis, co-eruptive and post-eruptive intervals. We also tested the efficacy of another approach, stacking, which, like time-series analysis, processes multiple SAR images together instead of as individual pairs to estimate displacement more accurately. Stacking involves adding the unwrapped phase of many consecutive date interferograms to increase their signal-to-noise ratio, by enhancing persistent deformation and suppressing random signals such as atmospheric noise (Pinel et al., 2014). However, this method has the limitation that it only offers the cumulative displacement for the full stack period and no details on the evolution of surface deformation over time. We stacked all the consecutive date interferograms for each of the 3 intervals to produce total displacement stacks for each interval, for each sensor. These stacks were compared against the long interval interferograms and time-series maps to gauge the performance of the stacking approach.

2.3. Seismicity

A total of four seismic stations were intermittently active between the end of 2019 and the end of 2022 at Pacaya (Fig. 2). PCG and PCG2 are short period stations. PCG4 is a broadband station, and PCG5 started as broadband and switched to short period in January 2022. Below, we describe the two different assessments we performed with these data: Real-time Seismic Amplitude Measurements (RSAM) and ambient noise cross-correlations.

2.3.1. RSAM

The amount of energy recorded by seismic stations can be used to infer the state of activity at volcanoes and forecast eruptions (Endo and Murray, 1991). This idea of leveraging the mean amplitudes of seismic records, through RSAM, was introduced by Endo and Murray (1991) to overcome the inaccuracies in estimates of seismic energy released before eruptions due to the inability to count earthquakes and measure coda lengths. RSAM also accounts for long-duration tremor signals which often accompany pre-eruptive and eruptive activity. At nearby Fuego volcano, for example, Naismith et al. (2019) found that peaks in the RSAM data correlated with the timing of paroxysmal eruptions, showcasing the use of these data for tracking changes in eruptive activity. At Pacaya, INSIVUMEH reports also suggest a close relation between explosive vigor and RSAM values.

We generated RSAM time-series from the four stations shown in Fig. 2 to assess whether peaks in RSAM corresponded to changes in activity during the 2021 eruptive crisis or to trends in the ground deformation. To exclude sources more likely to be associated with non-volcanic phenomena such as anthropogenic or meteorological noise, RSAM values are calculated for separate pre-defined 'useful' frequency bands in volcanic environments: this is termed Spectral Seismic Amplitude Measurements (SSAM) (Stephens et al., 1994; Tárraga et al., 2006; Krischer et al., 2015). The RSAM and SSAM for 3 band subsets (0.1–2 Hz, 1–5 Hz, and 5–10 Hz) were computed using the python-based SSxM obspy function (https://github.com/ThomasLecocq/ssxm). The data were first demeaned and bandpass filtered, and each value was then calculated on a 10-min window. Most seismic events associated with volcanic systems fall within the 0.1–8 Hz range (Power et al., 1996). Volcanic tremor is a continuous seismic signal that does not allow for individual events to be identified, with energy typically distributed non-uniformly in the 1–5 Hz band (Stephens et al., 1994; Cornelius and Voight, 1996; Power et al., 1996). Long-period events (LPs) are low-frequency signals typically in the 0.2–5 Hz range, whereas volcano-tectonic (VT) events peak from 5–15 Hz and are typically interpreted as capturing mechanical failure and tensile opening modes in the edifice (Clarke et al., 2021). Thus, the key band capturing volcanic seismic signals such as LPs and tremor is the 1–5 Hz band, but since other sources can also produce signal in that range, we compared results against the 5–10 Hz band to identify local earthquakes (VT events), and to the 0.1–2 Hz to identify teleseisms (distant earthquakes) (Stephens et al., 1994; Clarke et al., 2021).

2.3.2. Ambient Seismic Noise Cross-correlations

An alternative approach to leveraging seismic signals to track changes at volcanoes, seismic interferometry, relies on scattering of seismic waves due to heterogeneities in the crust (De Plaen et al., 2016). Cross-correlating these random wavefields recorded by two stations measures the impulse response of the medium at one station, as if the source was located at the other, that is the Green functions, from which temporal perturbations can be obtained to produce time-series of seismic velocity changes (Brenguier et al., 2008; De Plaen et al., 2016; Donaldson et al., 2017). Thus, velocity changes as small as 0.1% due to changes in pressure, heat, or water saturation in the ground can be retrieved (De Plaen et al., 2016). In volcanic regions, seismic ambient noise interferometry can exploit volcanic tremor as a source (De Plaen et al., 2016; Donaldson et al., 2017), but this also means that large variations in volcanic tremor can result in instabilities in the correlations. Typically, cross-correlation functions are calculated for different pairs of stations and the results are combined across a full network of stations to produce more stable results (De Plaen et al., 2016). However, this approach requires dense seismic networks, or at the very least two stations to be acquiring data in tandem. Recently, single station methods that were applied to the study of earthquakes have been validated for the study of volcanoes (De Plaen et al., 2016). At a single station, two types of cross-correlation can be performed: cross component (SC), where each component (north (N), east (E), vertical (Z)) is cross-correlated with a different one, or autocorrelation (AC), where each component is cross-correlated with itself, yielding 6 total combinations: NN, EE, ZZ,

EN, EZ, NZ. De Plaen et al. (2016) showed that at Piton de la Fournaise volcano (Réunion), both SC and AC were able to detect pre-eruptive seismic velocity drops as well as climate-related changes, particularly in the 1–2 Hz and the 0.5–1 Hz frequency bands, with SC results being more stable, and AC results being more sensitive to strong-amplitude transient events.

We performed seismic noise interferometry using the open-source software MSNoise (Lecocq et al., 2014), following the methods of Lecocq et al. (2014) and De Plaen et al. (2016). Only PCG2 and PCG5 were active consistently enough during the 2020–2021 study period so we restricted our analysis to these two datasets (Figs. S9 and S10). We focused on PCG5 broadband data for two intervals with the least gaps: October 3, 2019 to October 17, 2020, which corresponds to the 2021 pre-crisis interval, and January 18, 2021 to August 27, 2021, which spans parts of the co- and post-eruptive intervals. We also focused on PCG2 data between February 21, 2021 and January 18, 2022, which begins partway through the co-eruptive interval and continues into the post-eruptive interval. We applied the single station approach individually for these two PCG5 and one PCG2 subsets.

All data were pre-processed using a 0.01–8 Hz bandpass filter and resampled to 20 Hz. Spectral whitening was applied in all cases except AC, since this sets the amplitude of the signal to 1 and no useful information would remain (De Plaen et al., 2016), and the time-domain normalization was set to 1-bit. Processing was performed in 6 different frequency ranges, the 4 used by De Plaen et al. (2016): 0.01–1.0 Hz, 0.5–1.0 Hz, 1.0–2.0 Hz, and 2.0–4.0 Hz, and an additional two: 0.5–2 Hz and 0.5–3 Hz.

We computed the cross-correlation and autocorrelation for each day, for all possible components (NN, EE, ZZ, EN, EZ, NZ) and for all 6 filters, and applied a 15-day linear stacking to increase the signal-to-noise ratio.

Assuming homogeneous changes in the medium, the relative travel time differences (dt) are considered due to changes in seismic velocity (dv) (Lecocq et al., 2014), such that:

$$\frac{dv}{v} = -\frac{dt}{t} \tag{1}$$

These temporal velocity variations were measured in the negative and positive sides of the correlation functions, between 5 and 35 s time lags, and each individual daily correlation function was compared to a reference. Following De Plaen et al. (2016), we set the reference for each dataset as the average result for the whole time period of that dataset. The Multiple-Window Cross-Spectral Analysis method was used to measure travel time changes in the frequency domain, using a coherence of 0.65 as cut-off for quality control.

3. Results

3.1. Lava Flow Maps

On October 20, 2020, vents opened away from the summit area for the first time during the active period, which began in 2015. Thereafter, vents continued to open along most of the upper flanks of Pacaya, within the collapse scarp, as shown in Fig. 4. Based on changes in the spatial distribution of lava effusion throughout the eruptive sequence we categorized the flows into 5 groups and plotted each group as a different color (Fig. 4). More detailed descriptions of these observations are included in the Supporting Information (Section S1), as well as a figure with flows for each epoch plotted in different panels (Fig. S1). Areas covered by the lava flows during each epoch as well as approximate volumes are listed in Table S1. A link to the lava flow shapefile repository is also provided in the Supporting Information.

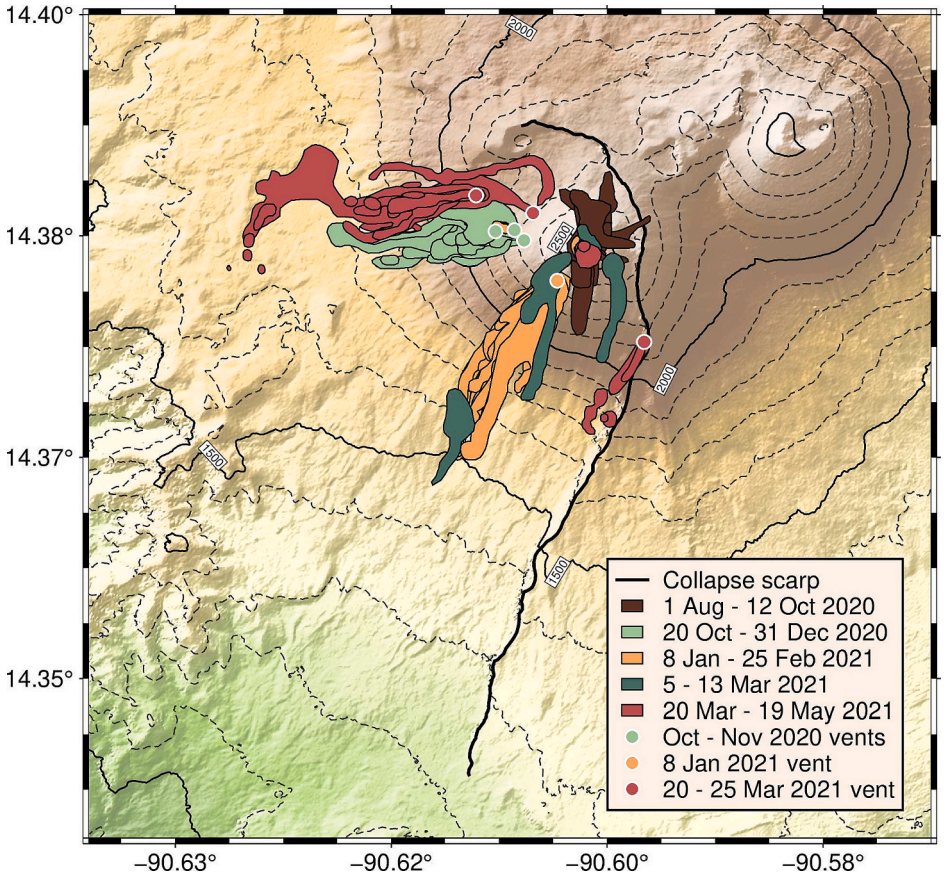

Fig. 4. Map of vent locations and lava flows erupted on Pacaya between October 2020 and May 2021, color-coded to highlight changes in effusive sources over the study period. Each of the epochs are also plotted in separate panels in Fig. S1 (Supporting Information).

3.2. August 1 – October 12, 2020

From August through September, we observed near-persistent crater incandescence and occasional lava flows, extending a few hundred meters away from the main summit. These flows are shown in brown in Fig. 4.

3.3. October 20 – December 31, 2020

The first instance of a visible thermal anomaly with its source away from the summit was on October 20, 2020. Between then and the end of 2020, lava flowed from a series of vents ~500–800 m west of the summit vent, as shown in light green in Fig. 4. The longest thermal anomalies extended ~1300 m in November.

3.4. January 8 – February 25, 2021

On January 8, 2021, we observed a shift in lava flow activity onto the southwest flank, emanating from vents ~350 m southwest of the summit crater and with maximum observed lengths of ~1400 m on January 9, and ~1700 m on February 25. At the end of January, crater incandescence was still observed, as well as a potential reactivation of the November 25/28 vents west of the summit. These flows are depicted in orange in Fig. 4.

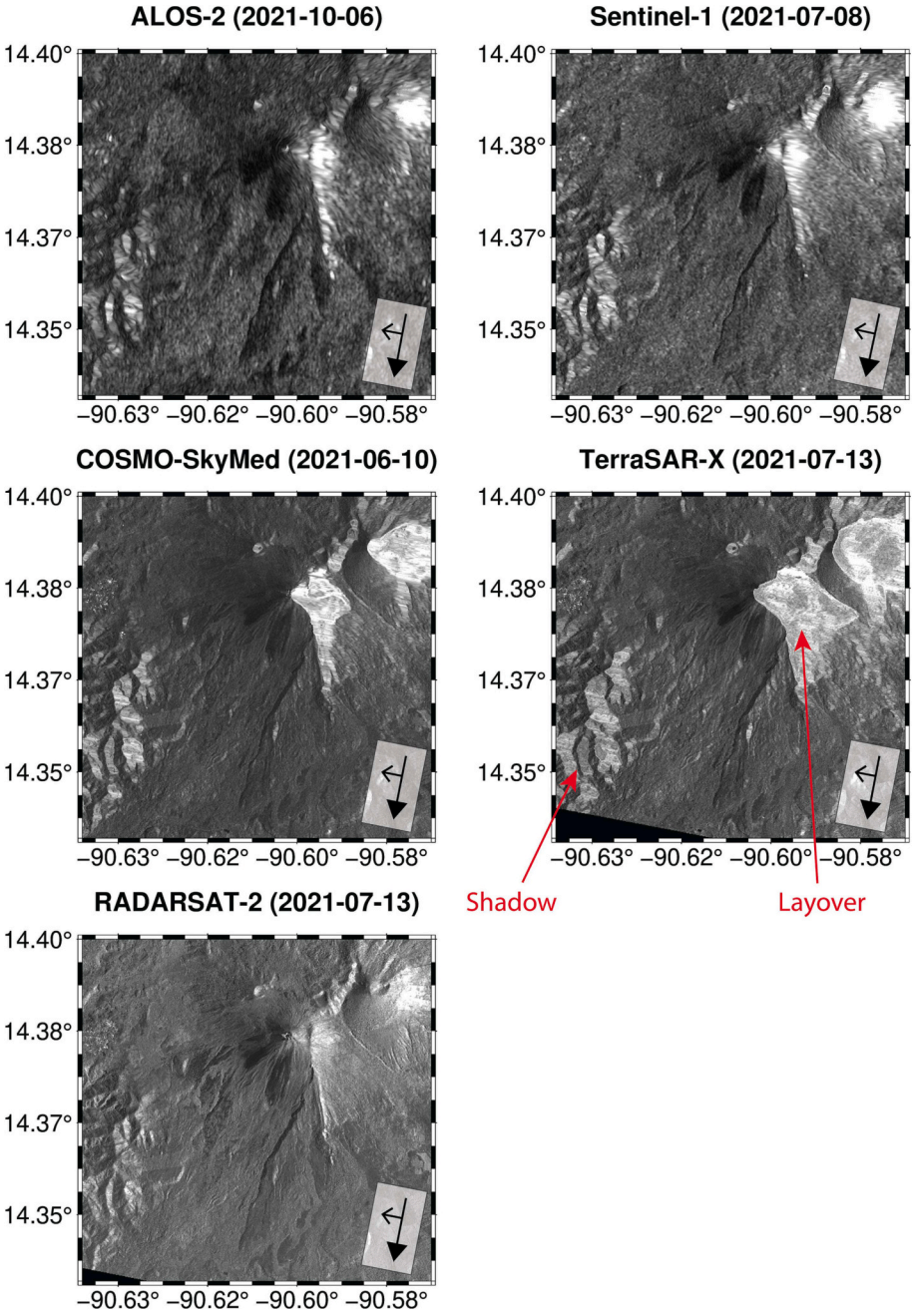

Fig. 5. Comparison of descending orbit amplitude data from ALOS-2, Sentinel-1, COSMO-SkyMed, TerraSAR-X, and RADARSAT-2, with red arrows pointing to examples of shadow and layover geometric artifacts. The filled black arrow represents the satellite flight direction, while the open arrow shows the look-direction. RADARSAT-2 Data and Products © MDA Geospatial Services Inc.(2022) - All Rights Reserved. RADARSAT is an official trademark of the Canadian Space Agency. (For interpretation of the references to color in this figure legend, the reader is referred to the web version of this article.)

3.5. March 5–13, 2021

Multiple flows were active on March 5 and 13, 2021, as shown in dark green in Fig. 4. At least two branches flowed southwest and south-southwest from the January vent, with at least three others originating nearer the summit crater and flowing southwest, north and south. On March 13, lava flowed at least 2350 m southwest from the summit, which showed ongoing incandescence, although cloud-cover impeded making out the full anomaly.

3.6. March 20 – May 19, 2021

By March 20, 2021, lava effusion on the southwest flank had ceased. Summit incandescence was ongoing, and a new lava flow appeared ~900 m southeast of the summit, flowing within the collapse scarp. On March 21 a new flow initiated northwest of the summit, extending ~2250 m west by March 30, from a vent ~1000 m northwest of the summit. The north flow was active at least through April 9, and no longer incandescent by April 19, 2021. On April 22 crater incandescence was visible and on April 30 and May 8, vigorous incandescence was observed around the area of the March 2021 vents despite dense cloud cover. The last clear lava flow was observed on imagery from May 14, 2021, originating north of the summit and flowing west, north of the earlier March flow, and extending for at least 2200 m. These final flows are shown in red in Fig. 4. By May 19, 2021, incandescence was no longer visible in this area, in agreement with GVP reports of the final flow activity on May 17, 2021 (Global Volcanism Program, 2013).

3.7. Radar satellite data

3.7.1. SAR amplitude

We inspected the amplitude images for each of the 9 SAR datasets, to identify morphological changes in the crater and volcanic flanks. Figs. 5 and 6 show comparison geocoded amplitude images from each of the satellites in the descending and ascending orbits, respectively, for post-eruptive acquisition dates. SAR imagery is acquired on side-looking geometries, which introduces distortions, such as foreshortening, shadowing, and layover, particularly over mountainous areas (Simons and Rosen, 2015). Foreshortening happens on relief sloping toward the satellite, whereas sloping away from the satellite leads to lengthening. Layover is an extreme case of foreshortening that happens when the slope of the target, in this case Pacaya, is steeper than the satellite incidence angle, such that the upslope is viewed sooner than the downslope and the pixel order in the images appears reversed (Pinel et al., 2014). Shadowing arises when surfaces slope away from the sensor such that the radar beam cannot illuminate them. These effects are greater the smaller the satellite incidence angle, that is the angle between the LOS and the vertical (Massonnet and Feigl, 1998). Due to

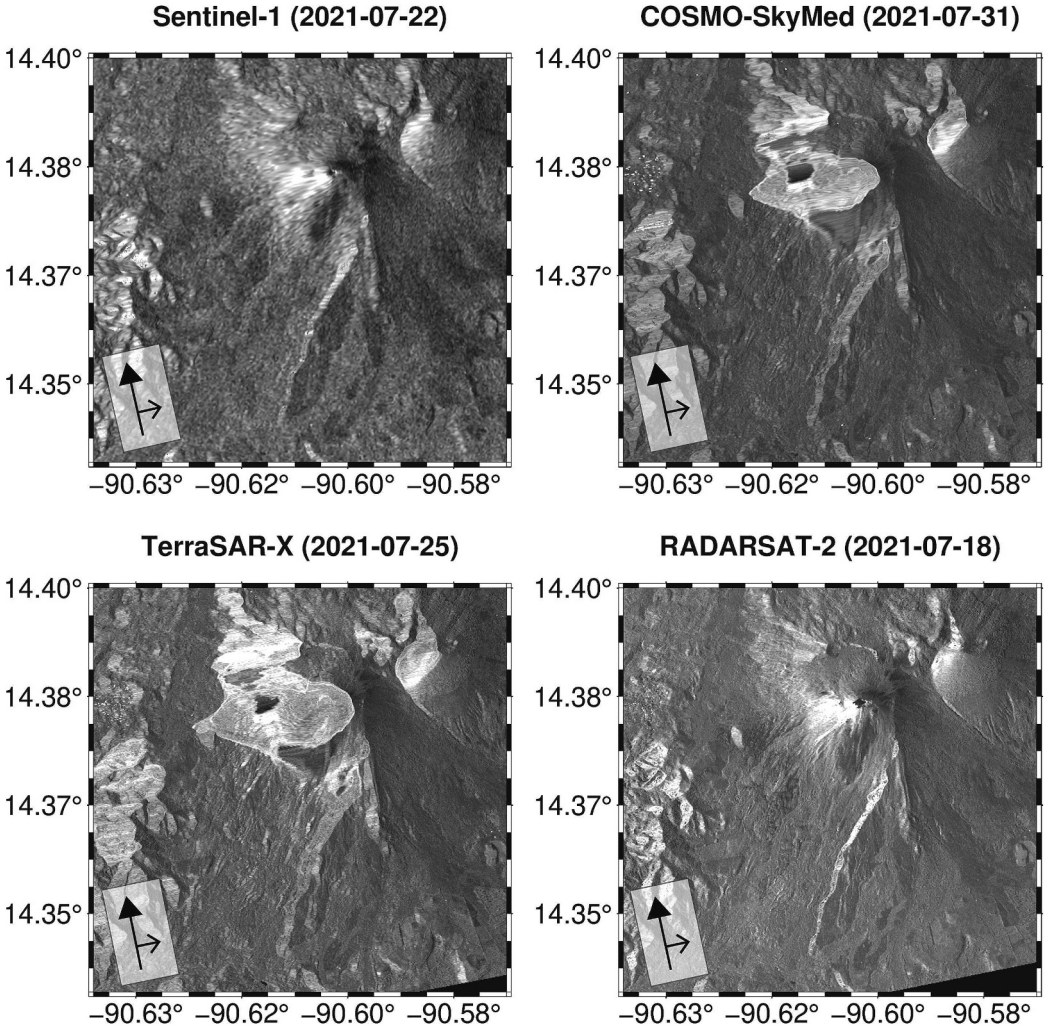

Fig. 6. Comparison of ascending orbit amplitude data from Sentinel-1, COSMO-SkyMed, TerraSAR-X, and RADARSAT-2. The filled black arrow represents the satellite flight direction, while the open arrow shows the look-direction. RADARSAT-2 Data and Products © MDA Geospatial Services Inc.(2022) - All Rights Reserved. RADARSAT is an official trademark of the Canadian Space Agency.

the shallow incidence angle of the TerraSAR-X (22–23°) and COSMO-SkyMed (24–27°) acquisitions, and the steepness near the summit at Pacaya, the ascending orbit scenes from these platforms show distortions on the western flank, and the descending orbit scenes show distortions on the eastern flank, extending to the summit crater region in both cases. Distortions are less extreme for the RADARSAT-2 dataset. Detailed observations from each of the datasets including example figures of observed changes are provided in the Supporting Information (Section S2).

Overall, ALOS-2 amplitude images show low amounts of distortion, but low spatial resolution; Sentinel-1 amplitude images show low distortion and have average spatial resolution; COSMO-SkyMed amplitude images have better spatial resolution but worse distortions; TerraSAR-X Spotlight-mode amplitude images show even finer detail but greater distortions; and RADARSAT-2 spotlight-mode amplitude images have the best spatial resolution and least distortions of the high-resolution datasets in this study.

These data allow observation of crater changes in the summit around January 2021 and the appearance of a ~100 m long trough-like feature on the west-northwest edge of the crater on May 2021 (Sentinel-1: Fig. S3), the appearance of lava flow channel features on the southwest flanks (descending COSMO-SkyMed and TerraSAR-X: Figs. S4 and S6), and changes in the distorted regions that spatially match lava flow emplacement locations (ascending COSMO-SkyMed and TerraSAR-X: Figs. S5 and S7). The high-resolution datasets, such as RADARSAT-2, enable identification of lava flow channels that are only ~10 m across (Figs. 5 and 6).

3.7.2. Differential InSAR

Differential interferograms were created as inputs for time-series analysis and stacking, but also individually inspected. Fig. 7 shows an example co-eruptive interferogram from the descending orbit TerraSAR-X dataset, highlighting widespread loss of coherence, manifesting as pixelation, nearest the summit area as well as on the western flank. The latter closely matches the outline of lava flows emplaced during the time spanned by the interferogram. Despite the loss in coherence in the summit and lava flow regions, co-eruptive interferograms still displayed dense fringes on the west and southwest flanks (e.g., Fig. 7).

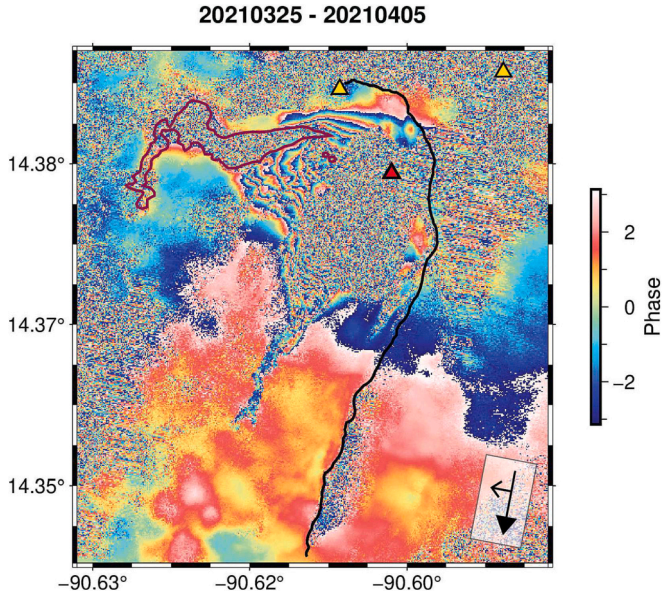

Fig. 7. Descending orbit TerraSAR-X wrapped interferogram from scenes acquired on March 25 and April 5, 2021, showing loss of coherence (pixelated appearance) where the lava flow observed on the March 30, 2021 imagery was emplaced (purple outline). We also observe a high density of fringes in the coherent areas directly surrounding the lava flow source and extending down the southwest flank. The black line represents the ancestral collapse scarp and the red triangle represents the Mackenney cone. The filled black arrow represents the satellite flight direction, while the open arrow shows the look-direction. (For interpretation of the references to color in this figure legend, the reader is referred to the web version of this article.)

Overall, interferograms showed better summit coherence before and after the heightened eruptive period, as shown by the descending orbit Sentinel-1 example in Fig. 8. The pre-crisis and post-eruptive interferograms also display summit fringes that match the locations of lava flow emplacement prior to their spanned time periods.

Fig. 9 shows an example interferogram with similar time in between acquisitions (72 to 84 days) for each dataset, enabling comparison of platform performance. COSMO-SkyMed and TerraSAR-X, both the X-band sensors, show the greatest loss of coherence, manifesting as pixelation, surrounding the volcanic edifice and in the regions affected by lava flow emplacement. Given the shallower incidence angles for both these datasets, coherence is also lost in regions of layover, which especially affects the ascending orbit data over the summit area. Sentinel-1 and RADARSAT-2, the C-band sensors, produce interferograms that retain more coherence than the X-band sensors, and ALOS-2, being L-band, preserves the most coherence, even extending beyond the volcanic flanks. RADARSAT-2, having higher spatial resolution than Sentinel-1, produces smoother-looking results. Despite ALOS-2 showing the best coherence, the coarser spatial resolution results in a grainier appearance for its output interferograms. Finally, since each fringe in an interferogram corresponds to a phase change of half the radar wavelength, we observe the most fringes in the X-band data and the least in the L-band data.

3.7.3. Stacking

Consecutive unwrapped interferograms for each of the 9 datasets were stacked into pre-crisis, co-eruptive and post-eruptive stacks (if data for those dates were available) and compared against the respective long interval unwrapped interferograms made from the start and end acquisitions in each stack (Figs. 10 and S11–S18). Fig. 10 showcases how the stacked maps for the descending Sentinel-1 example have increased signal-to-noise ratio compared to the long interval interferograms, which are affected by loss of data (pixelated areas indicating low coherence) due to temporal decorrelation. The stacked data show negative LOS displacements of up to 100 cm in the summit and neighboring areas, where coherence is lost in the long interval interferograms, with the peak displacements tracking the location of lava flow emplacement shortly before and during each interval. Comparisons for all other datasets are included in the Supporting Information (Figs. S11–S18). Given the few ALOS-2 interferograms to stack, this dataset shows the least improvement after stacking (Fig. S11). The Sentinel-1 data, on the other hand, show the clearest improvement (Figs. 10 and S12). The datasets affected by significant layover (COSMO-SKyMed and TerraSAR-X) show distortions in the affected areas regardless of stacking (Figs. S14 and S16).

3.7.4. InSAR Time-series

Fig. 11 shows the LOS displacements obtained through individual SBAS time-series analysis on each dataset for the 10 by 10 pixel time-series region shown in Fig. 2, manually overlain onto the same plot. The time-series location was chosen as the highest elevation point on the southwest flank that remained coherent in all 9 datasets. Since all datasets were resampled onto the same DEM grid during conversion from SAR coordinates to geographic coordinates, the time-series location is equivalent in all datasets. Individual time-series plots for each of the datasets are included in the Supporting Information (Figs. S19–S27). We observe a general trend of decreasing LOS displacements (ground motion away from the satellites) through 2021, when the displacements reverse and start to follow a positive trend. There is good overlap between most datasets, except for the ascending orbit Sentinel-1 and COSMO-SkyMed datasets. Their deviation is most striking from the start

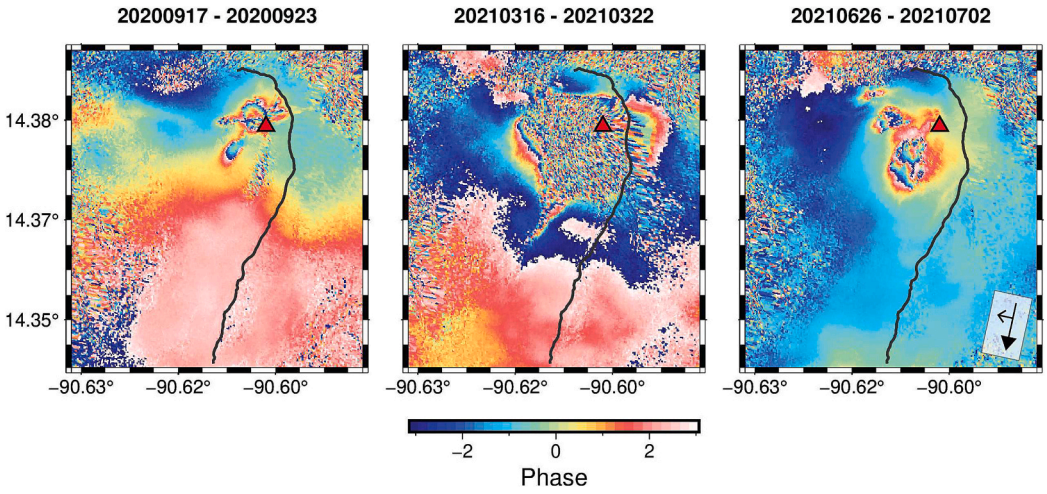

Fig. 8. Example pre-crisis (left), co-eruptive (middle), and post-eruptive (right) consecutive date wrapped interferograms from descending orbit Sentinel-1 highlighting a greater lack of coherence (more pixelation) near the summit during the co-eruptive period. The summit fringes in the pre-crisis and post-eruptive interferograms match the locations of prior lava flow emplacement (Fig. 4). The black line represents the ancestral collapse scarp and the red triangle represents the Mackenney cone. The filled black arrow represents the satellite flight direction, while the open arrow shows the look-direction. (For interpretation of the references to color in this figure legend, the reader is referred to the web version of this article.)

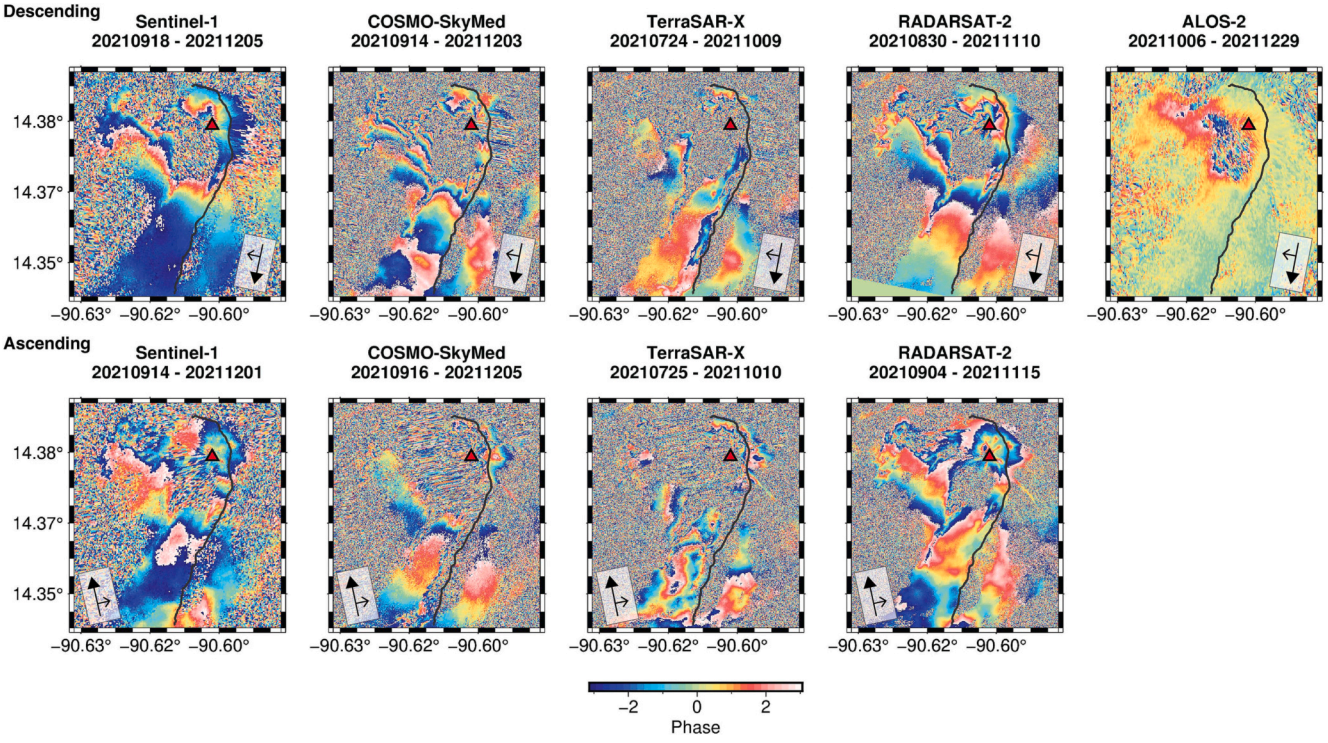

Fig. 9. Example descending (top) and ascending orbit (bottom) wrapped interferograms from all five platforms, spanning similar time frames between acquisitions (72 to 84 days). The black line represents the ancestral collapse scarp and the red triangle represents the Mackenney cone. The filled black arrow represents the satellite flight direction, while the open arrow shows the look-direction. RADARSAT-2 Data and Products © MDA Geospatial Services Inc.(2022) - All Rights Reserved. RADARSAT is an official trademark of the Canadian Space Agency. (For interpretation of the references to color in this figure legend, the reader is referred to the web version of this article.)

until the end of the eruptive period, when they follow a flatter trend than their respective descending datasets, but we see better agreement from mid-2021 onward.

The MSBAS results (Fig. 12) show a similar trend to the overlapping SBAS time-series (Fig. 11), with horizontal displacements showing westward motion starting with the co-eruptive period, on October 2020, accelerating at the start of the post-eruptive period until the end of 2021, and shifting to eastward motion thereafter. The vertical displacements show more scatter but appear to show downward motion during the co-eruptive period, which accelerates directly after, before flattening out after the middle-end of 2021.

The SBAS time-series approach is limited by the availability of well-connected networks of scenes and by the coherence of the individual interferograms from which the time-series are derived. Since we were interested in identifying changes between the pre-crisis, co-eruptive and post-eruptive intervals, and obtaining the best possible coherence in the

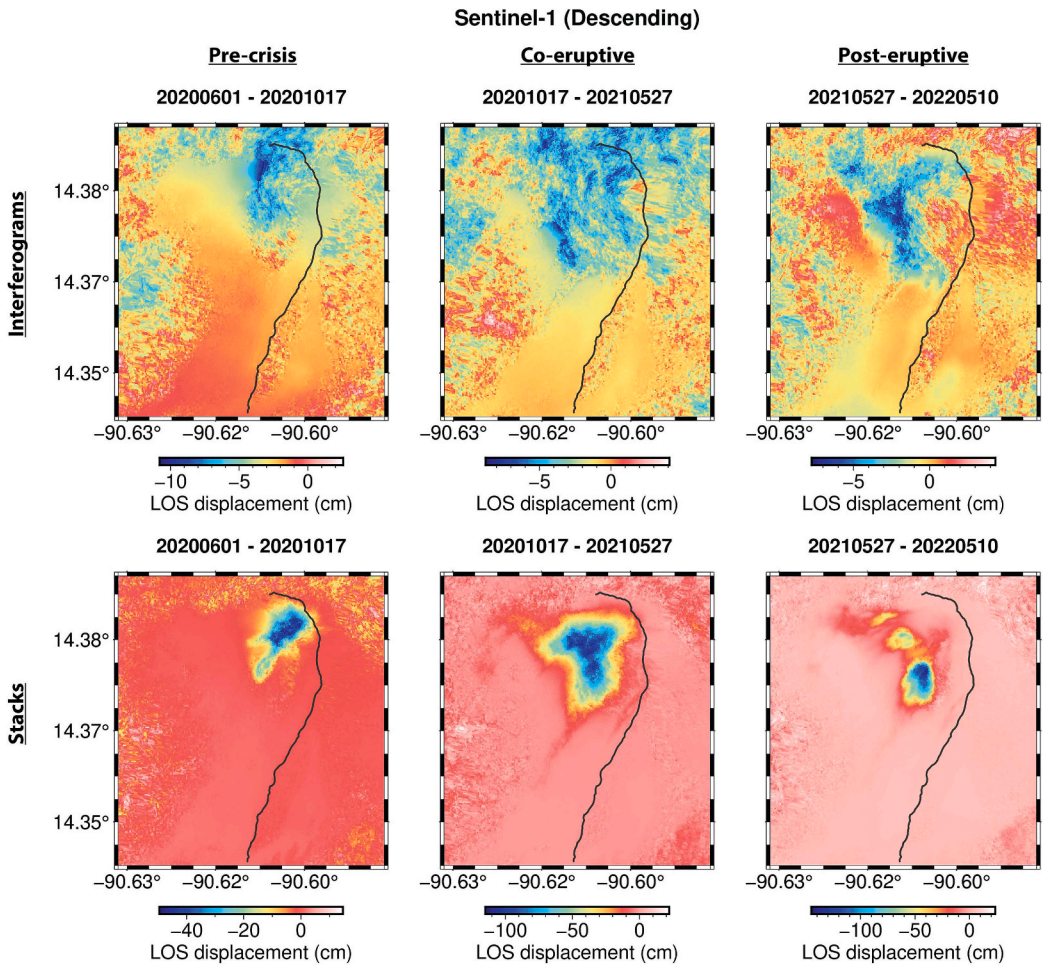

Fig. 10. Comparison of long interval unwrapped interferograms (top) and stacks (bottom) for the pre-crisis (left), co-eruptive (middle), and post-eruptive (right) descending Sentinel-1 data. The black line represents the ancestral collapse scarp and the red triangle represents the Mackenney cone. The filled black arrow represents the satellite flight direction, while the open arrow shows the look-direction. (For interpretation of the references to color in this figure legend, the reader is referred to the web version of this article.)

displacement maps, we reprocessed time-series for these shorter intervals, for those datasets where enough scenes were available (> 6). Otherwise, we extracted the interval displacements from the results of the full dataset time-series analysis. Fig. 13 shows pre-crisis, co-eruptive, and post-eruptive displacement maps derived from individual period time-series results for the example descending Sentinel-1 dataset. All other dataset maps are included in the Supporting Information (Figs. S28–S35). In all cases, loss of coherence, shown as no data, in white, is greatest in the summit areas. The Sentinel-1 maps highlight how changes in coherence vary greatly by interval (Fig. 13). The pre-crisis maps are mostly incoherent, or missing data, in the summit area which was affected by lava flows prior to October 2020; the co-eruptive map shows the greatest loss in coherence, or the greatest amount of missing data; and the post-eruptive map shows some improvement in coherence, as reflected by a greater abundance of pixels for which data was obtained.

3.8. Seismicity

3.8.1. RSAM

Fig. 14 compares the SSAM results from stations PCG2, PCG4 and PCG5 for the 0.1–2, 1–5, and 5–10 Hz bands. The individual plots for each station are included in the Supporting Information (Figs. S36–S38). Unfortunately, there are large data gaps in the seismic record (see Figs. S9 and S10) due to intermittent telemetry problems and a change from a broadband to short-period sensor at PCG5 in early 2022. PCG RSAM data only covered the end of 2021 and thus were not considered. There is a gap in data during the first half of the heightened interval, so we are unable to see whether there was a clear ramp-up in RSAM as lava effusion patterns began to change. However, we observe that the remainder of the heightened interval shows more peaks than the intervals before and after in all 3 frequency bands. There is a further peak in the PCG5 data in June, after the eruption, showing up strongest in the 0.1–2 Hz range, but this was not observed at the other stations. Besides this post-eruptive peak, the rest of 2021 shows similarly low RSAM values in the 1–5 Hz range to those observed before October 2020. There are some isolated peaks, the largest of which also appear in the lower and higher frequency bands. The 0.1–2 Hz range also shows an increase in peaks starting later in the co-eruptive period but this is not as marked in the other two frequency ranges.

3.8.2. Ambient seismic noise cross-correlations

Fig. 15 shows the mean and median plots for variations in seismic velocities derived from 15-day stacks of single-station AC and SC for the 2019–2020 PCG5 data, and the 2021 PCG2 and PCG5 data. Example AC and CC functions used to estimate the seismic velocity changes are provided in the Supporting Information (Figs. S39-S40). We observe good agreement between the AC and SC results for the 2019–2020 PCG5 data, with velocity variations between -0.2 and 0.2%, and peak velocities in the summer and troughs in the winter. The 2021 results from

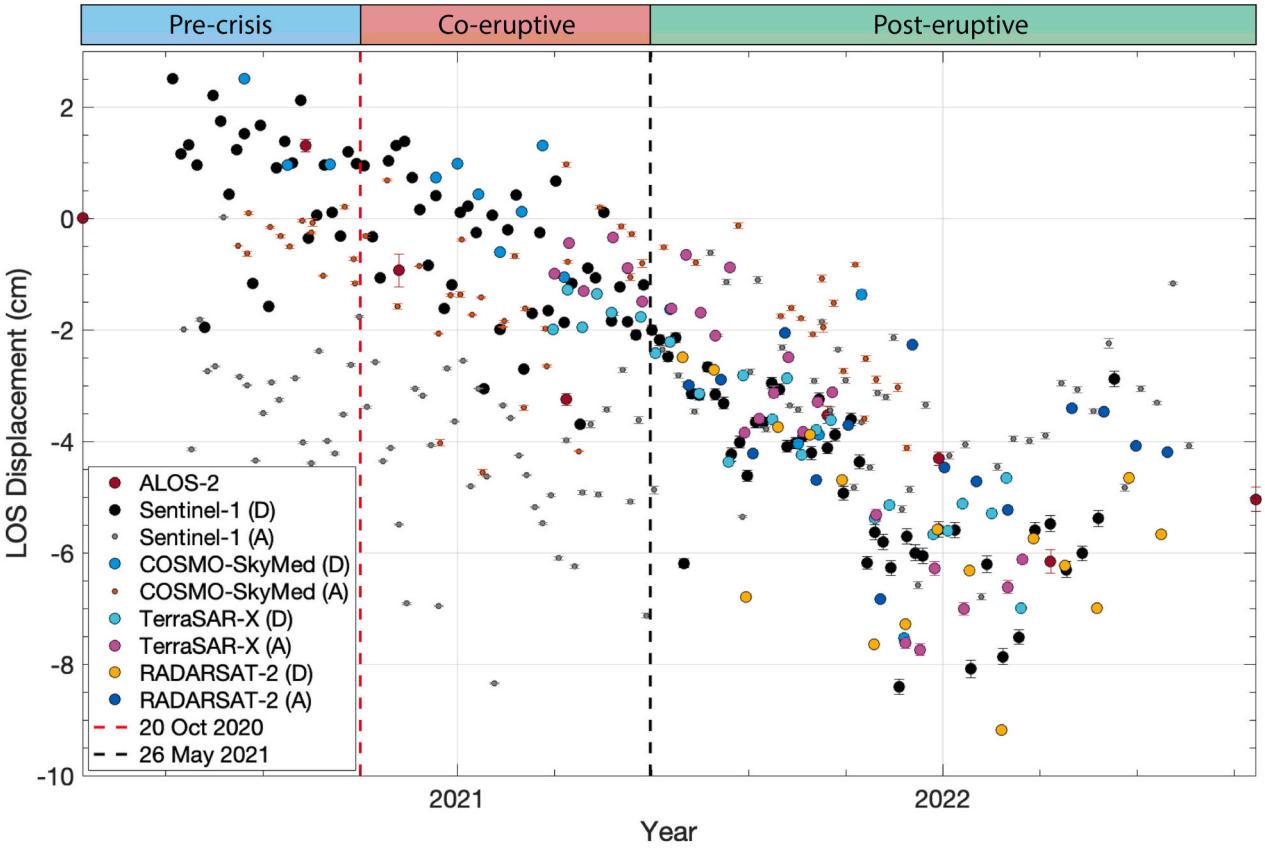

Fig. 11. SBAS time-series for all 9 datasets manually overlaid on the same plot. Negative Line Of Sight (LOS) displacements represent motion of the ground away from the satellite. Ascending Sentinel-1 and COSMO-SkyMed datasets are plotted as smaller icons, since they show the least fit to the overall trend. The error bars represent the standard deviation in displacements amongst the 10 × 10 time-series pixels. The vertical red dashed line marks the timing of first vent opening beyond the summit crater on October 10, 2020, and the dashed black line marks the timing of the final ash venting recorded on May 26, 2021. The top bar showcases the timing of the pre-crisis, co-eruptive, and post-eruptive intervals referred to in the text. Individual time-series plots are included in the Supporting Information (Figs. S19–S27). (For interpretation of the references to color in this figure legend, the reader is referred to the web version of this article.)

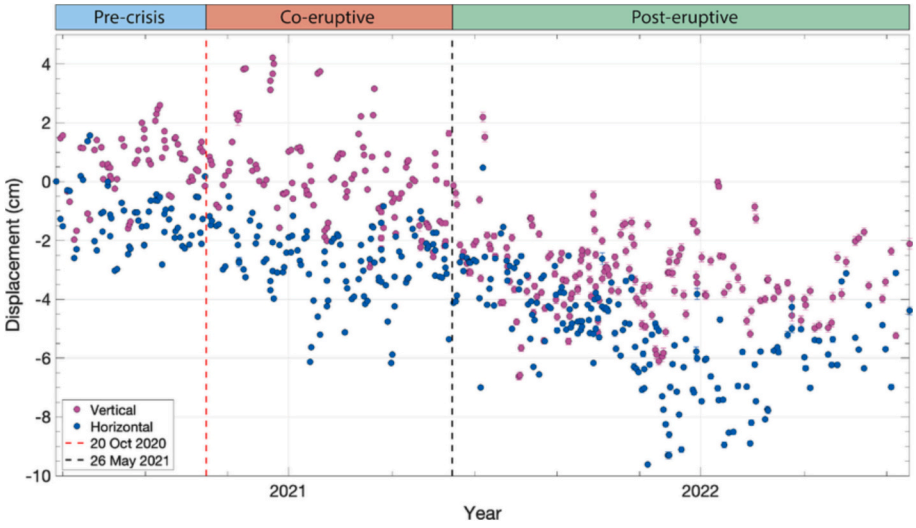

Fig. 12. MSBAS time-series of the vertical (pink) and horizontal (blue) displacement components calculated from all 9 InSAR datasets. Negative vertical displacements correspond to downward ground motion and negative horizontal displacements correspond to westward motion. The error bars represent the standard deviation in displacements amongst the 10 × 10 time-series pixels (these are smaller than the symbols wherever not visible). The vertical red dashed line marks the timing of first vent opening beyond the summit crater on October 10, 2020, and the dashed black line marks the timing of the final ash venting recorded on May 26, 2021. The top bar showcases the timing of the pre-crisis, co-eruptive, and post-eruptive intervals referred to in the text. (For interpretation of the references to color in this figure legend, the reader is referred to the web version of this article.)

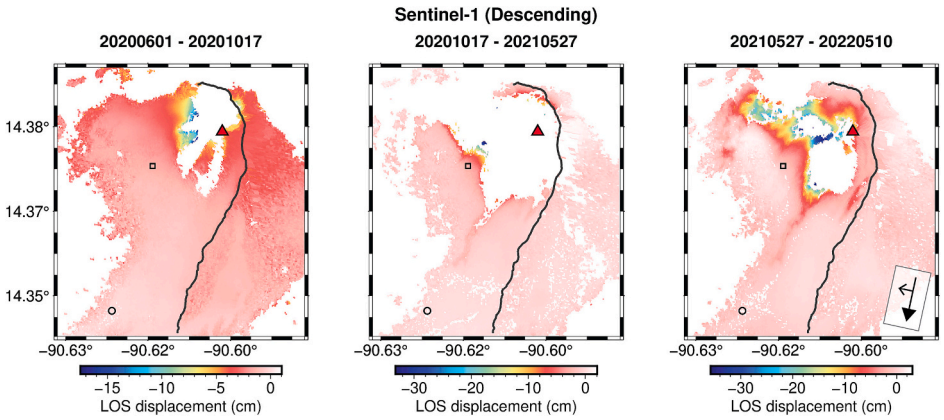

Fig. 13. Descending Sentinel-1 cumulative displacement maps spanning the pre-crisis (left), co-eruptive (middle), and post-eruptive (right) intervals, obtained from individual SBAS time-series analysis for each interval. The black circle outlines the location of the reference point, and the black square shows the location of the time-series point. No data regions, in white, are those where the coherence was below the chosen 0.3 threshold in at least 1 of the interferograms used in SBAS time-series analysis. The black line represents the ancestral collapse scarp and the red triangle represents the Mackenney cone. The filled black arrow represents the satellite flight direction, while the open arrow shows the look-direction. (For interpretation of the references to color in this figure legend, the reader is referred to the web version of this article.)

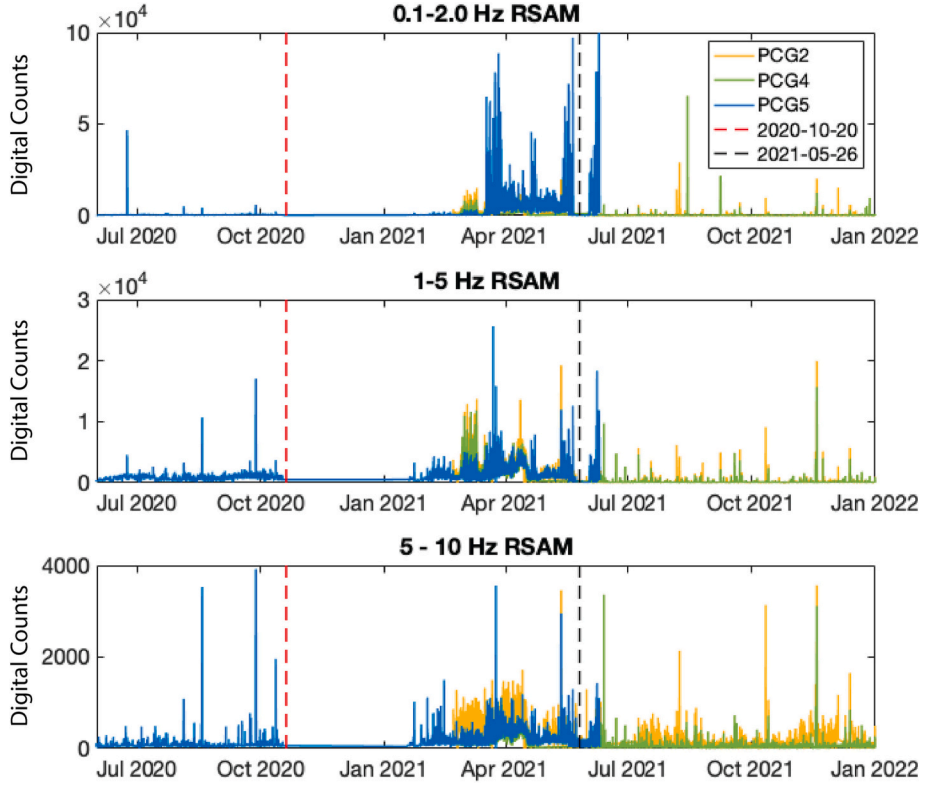

Fig. 14. SSAM plots for stations PCG2 (yellow), PCG4 (green) and PCG5 (blue) and frequencies of 0.1–2 (top), 1–5 (middle) and 5–10 Hz (bottom). The red and black vertical dashed lines show the start and end of the heightened eruptive interval, respectively. Note the gap in data between the end of October 2020 and the end of January 2021. (For interpretation of the references to color in this figure legend, the reader is referred to the web version of this article.)

both stations are noisier and harder to interpret, but overall, both AC plots and both SC plots look similar to each other. AC data for PCG2 appear less noisy than for PCG5. Both 2021 SC results show lower variability at the start and increased variability at the end of the periods. For PCG5, this begins in April 2021, intensifying after July, whereas for PCG2 the larger peaks appear after November 2021.

4. Discussion

4.1. Interpretation of the deformation signals

Pacaya experienced several changes in flank displacement rates throughout the 2021 eruptive period (Figs. 11 and 12). Before and during the heightened activity period, we observe larger discrepancy between the ascending and descending datasets (Fig. 11), with descending data showing negative LOS motion trends, while the ascending data show a flatter trend. All LOS results as well as the

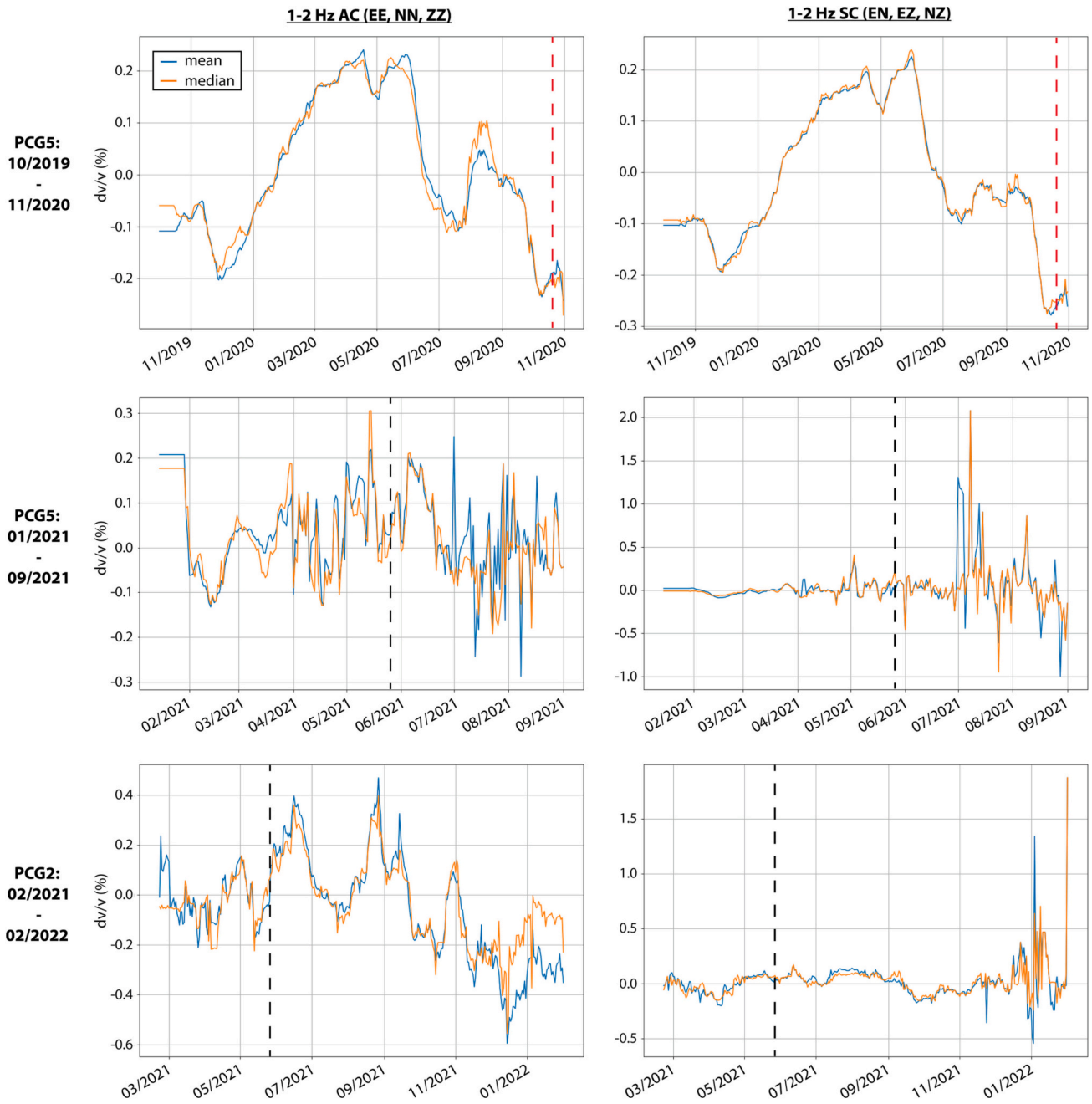

Fig. 15. Variation of the 15-day averaged seismic velocity for both PCG5 subsets (top and middle) and PCG2 (bottom) for the 1–2 Hz frequency range measured using single-station autocorrelation (AC – left) and cross-components (SC – right). The blue and orange lines represent the mean and median results, respectively, for the three components considered for each plot, and the red and black vertical dashed lines show the start and end of the heightened eruptive interval, respectively. (For interpretation of the references to color in this figure legend, the reader is referred to the web version of this article.)

horizontal displacements show a change in trend at the start of 2022, with LOS displacements becoming positive, and horizontal motion switching from westward to eastward, whereas vertical displacements show a more subtle change to a flatter trend starting sooner.

Given the evidence for previous flank creep at Pacaya also corresponding to times of lava effusion from vents beyond the summit crater (Gonzalez-Santana et al., 2022), a likely candidate for the observed negative LOS displacement trend is flank creep. This is compatible with the motion components being downward and westward displacements, since this corresponds to down-dip motion on a southwest flank. Additionally, the total ~10 cm negative LOS displacement in descending orbit datasets observed for the time-series location on the southwest flank (Fig. 2) is comparable to the magnitude observed in similar time-series spanning the previous transient instability events in 2010 and 2014 (Gonzalez-Santana and Wauthier, 2021; Gonzalez-Santana et al., 2022). It should be noted that all the displacements presented here are values for the time-series location, which was chosen based on the constraint that SBAS time-series only produce results for pixels that remain coherent in all input interferograms. As such, these are not maximum values, and locations further up the flank could have experienced greater displacements, like the ones reported for the 2010 instability event (Schaefer et al., 2015). Additionally, given the complex nature of the observed deformation patterns, likely overprinting from other signals, and the lack of coherence near the summit, we consider physical modeling of potential deformation sources to be beyond the scope of this paper.

InSAR time-series leading up to the start of the heightened activity period studied here showed flank displacement rates of ~1.2 cm/yr from 2015 to 2018, followed by negligible displacements from 2019 through the end of 2020 (Gonzalez-Santana et al., 2022). Joint time-series analysis of the descending Sentinel-1 dataset presented in Gonzalez-Santana et al. (2022) and that presented here suggests that the observed trend of decreasing LOS displacements initiated concurrently with the start of the heightened eruptive interval around October 2020. There is evidence for flank movement between 2015 and 2019, followed by negligible displacements between 2019 and 2021 (Fig. S41). Flank movement then renews with eruptive activity in 2021. Thus, the initiation of this new transient flank instability event corresponded in time with the initiation of a heightened eruptive period characterized by lava effusion beyond the summit crater, as in 2010 and 2014.

There are two other possible factors impacting displacement signals at Pacaya. The first is seasonal variability in tropospheric water vapor, which can cause scatter in time-series, particularly in tropical settings such as Guatemala (Ebmeier et al., 2013). As shown in Gonzalez-Santana et al. (2022), this variability can cause annual oscillations in InSAR time-series data at Pacaya, with amplitudes of ~2.5 cm and peaks in the high rainfall months of boreal summer, and troughs during the drier boreal winter. Thus, the 5 cm uptick observed in 2022 might be related to the effect of variations in tropospheric water vapor, and not a true shift in the direction of motion. Displacements prior to 2022, however, are of a greater magnitude, and thus more likely to be a true signal that is large enough to overprint the cyclical tropospheric water vapor variation trend.

The second possible factor is lava flow compaction or settling of volcanic material such as tephra. As can be seen in the stacked displacement maps (e.g., Fig. 10), there is considerable negative LOS motion over areas where lava flows have been emplaced (Fig. 4), with magnitudes of up to ~100 cm. The 2021 eruption had a larger area inundated by lava flows than the two previous eruptions, with some flowing either side of the chosen time-series point. Since the time-series point was chosen to remain coherent in all 9 datasets across their full durations, and we observed a loss of coherence in interferograms spanning a new emplacement of lava, it is unlikely that the chosen point is directly on a lava flow. Thus, there is a low likelihood of the signal directly capturing lava flow compaction. Briole et al. (1997) found that subsidence can extend outside lava flows, likely due to relaxation of the substrate in response to loading produced by the emplaced lavas, based on their study at Etna volcano (Sicily). Through numerical models, they were able to estimate that the amplitude of the expected lateral bulging would be <10–15% of the maximum subsidence. Thus, it appears that substrate relaxation would have primarily a vertical component, whereas here we observe both horizontal and vertical displacements of similar magnitudes (Fig. 12).

Despite the similarities in volcanic activity and flank displacements for this eruption and those in 2010 and 2014, this eruptive crisis was followed by a striking change in the direction of flank displacement at the start of 2022, from negative to positive LOS displacements and westward to eastward horizontal displacements. After the 2010 eruption, negative LOS displacements decayed over 3 years until the 2014 eruption, while after the 2014 eruption, the negative LOS displacements decayed over approximately another 3 years before leveling out right until this 2021 eruptive crisis. The 2021 flank motion only lasted for 6 months after the end of the eruption, before the change in trend. Possible explanations for such a reversal in ground displacements could be deflation of the flank post-eruption, which would likely cause larger horizontal than vertical displacements, as observed. This switch in LOS motion marks a change in the behavior of flank displacements at Pacaya since the start of the time-series presented in Gonzalez-Santana et al. (2022). The study period presented here only just captures the start of this shift, therefore, time-series should be extended in future work, in order to better understand the possible mechanisms at play, as well as any implications for changes in flank motion in the future.

The time-series results presented here show a third occurrence of renewed or accelerated flank displacements at Pacaya during vigorous eruptions since 2007 (Schaefer et al., 2015; Gonzalez-Santana and Wauthier, 2021; Gonzalez-Santana et al., 2022). Importantly, this has happened in all three instances of vent opening beyond the summit crater over that time interval (Gonzalez-Santana et al., 2022), suggesting that we can expect more flank instability at Pacaya with more of these styles of eruption, which is an important observation for forecasting the likelihood of future flank displacement events. However, we note the small sample size of only three events and the variability in SAR data available over each event due to changes in the number and types of SAR satellites in orbit. There are additional differences between the characteristics of the volcanism accompanying each event. The 2010 eruption was accompanied by the greatest and most extensive amount of flank displacement and was also the only one where lava flow vents opened outside the collapse scarp (Schaefer et al., 2015). Both the 2014 and 2021 eruptions had lava flowing from vents within the collapse scarp instead. The 2014 eruption had lava effusion from 2 main vent locations, west and south of the summit, whereas the 2021 eruption had vent locations to the west, southwest and south. Additionally, the 2010 and 2021 eruptions were both directly preceded by volcanic activity from the main summit, whereas the 2014 eruption took place following relative volcanic quiescence (Wnuk and Wauthier, 2017; Gonzalez-Santana and Wauthier, 2021).

4.2. Insights into the performance of different satellite platforms and processing techniques

Overall, we note the advantage of high spatial resolution data for identifying small-scale changes on volcanic flanks. In this study, this included imagery in Spotlight mode from RADARSAT-2 and TerraSAR-X and in Stripmap mode from COSMO-SkyMed. The Sentinel-1 constellation provides the best temporal resolution data, with average spatial resolution, and has a more reliable repeat pass interval, like RADARSAT-2. ALOS-2 data have the least reliable repeat pass interval, and the coarsest spatial resolution, however the longer wavelength increases the potential to produce coherent interferograms over vegetated areas, particularly for interferogram pairs with longer temporal baselines. Sentinel-1 has the further advantage of consistently acquiring data in the path/frames established since both A and B platforms were launched and fixed, whereas other sensors, such as RADARSAT-2 and TerraSAR-X, rely on tasking for data to be actively collected over certain regions in the world, especially in the high-resolution Spotlight imaging mode. Since it can take time to set up acquisition requests, this resulted in no available imagery covering the start of the eruptive crisis from the tasked platforms. The availability of imagery acquired with larger incidence angles was beneficial for minimizing geometric distortions, especially layover, on the steep flanks of Pacaya. This led to Spotlight-mode RADARSAT-2 imagery slightly outperforming relative to the other high resolution datasets. Thus, whenever satellites have many incidence angles available for tasking, the tasker should consider the trade-offs between a timelier tasking versus one with the appropriate incidence angle and flight direction specifications to appropriately capture data over the slopes of interest.

In terms of processing approaches, we find that even when shorter time-series could be processed for each eruptive interval (e.g., Sentinel-1), stacking performed better than extracting cumulative displacements from the time-series (Figs. 10 and 13), as far as retaining more data in the summit and other fast changing areas. However, time-series analysis enables tracking the evolution of the displacement of each coherent pixel over time, whereas stacking only provides an absolute change for the full interval. Nevertheless, both of these approaches perform better than the conventional differential interferogram, especially when looking at long periods of time, since temporal decorrelation reduces coherence. Loss of coherence is particularly challenging in active volcanic regions, since it can arise due to emplacement of lava flows and

falling ash, which alter the back-scattering properties of the surface. Large displacements can also lead to phase gradients greater than a fringe per pixel, which also results in incoherence. Therefore, wherever large displacements are expected, shorter time interval interferograms or longer wavelength data are beneficial for retaining the most coherence.

Comparison of similar time interval interferograms from each dataset further highlights the interferometric performance and sensitivities of each platform (Fig. 9). Overall, we see the least phase change in the ALOS-2 data, given the longer wavelength, but also the most data closest to the summit, in regions affected by lava flow compaction. COSMO-SkyMed and TerraSAR-X perform similarly, retaining the least coherence, but showing the most fringes in coherent areas, due to the shorter wavelength of their sensors (X-band). Given their shallow incidence angles, coherence is lost in regions of layover, which especially affects the ascending orbit data over the summit area. RADARSAT-2 operates at the same wavelength as Sentinel-1 but has a finer spatial resolution, so captures a cleaner signal in its interferogram.

The emplacement of lava flows changes the surface scattering properties of the ground such that coherence is often lost in interferograms where the first image was acquired prior to emplacement (Fig. 7). Thus, the appearance of incoherence can be used to track lava flow emplacement. We observed this coherence loss in all datasets, but most starkly in the shorter wavelength datasets, as seen when comparing the co-eruptive time-series maps for the L, C, and X-band data (e.g., Figs. S28, 13, and S30, respectively). Interferograms showed better coherence before and after the heightened eruptive period, likely because conditions remained more stable and there was less frequent ash fall (Fig. 8). After emplacement, lava flows cool and compact over time, which can be captured as deformation fringes in interferograms, especially since recently emplaced flows tend to be coherent due to an absence of vegetation. This is seen after June 2021 in the region of the northwest flows (Fig. 13). Thereby, wherever lava flows have been emplaced, the assessment of whether there are any additional sources of deformation is complicated.

4.3. Interpretation of the seismic signals

The lack of long-term continuity in the seismic data for Pacaya prevents us from being able to create full time-series of RSAM or velocity variations to fully capture changes during the pre-crisis, co-eruptive, and post-eruptive intervals.

Nevertheless, in the RSAM data, we observe more peaks during and shortly after the co-eruptive period across all frequency ranges (Fig. 14). For the 1–5 Hz range that is expected to capture magmatic activity, we also observe higher values during the pre-crisis period, where lava effusion was ongoing from the summit crater, than for the post-eruptive period, where lava effusion had stopped. Thus, RSAM values do appear to reflect vigor of magma effusion at Pacaya. Unfortunately, given the break in data at the time of first vent opening away from the summit in late October 2020, we are unable to infer whether the larger RSAM peaks in the second half of the co-eruptive period for which we have data might be due to a difference in the location of lava effusion or simply due to the increased vigor of lava effusion and explosive activity.

Given the findings by Liu et al. (2019) that seismic velocity variations can track changes in rainfall, we produced a time-series of rainfall data to compare to the velocity variations (Fig. 16). We used Global Precipitation Measurement Mission (GPM) Level 3 Integrated Multi-satellitE Retrievals for GPM (IMERG) Final Daily 0.1 × 0.1° data obtained from the Goddard Earth Sciences Data and Information Services Center through their GIOVANNI visualization tool (https://giovanni.gsfc.nasa.gov/giovanni/), which provide an estimate of daily accumulated precipitation (Huffman et al., 2019). Data were downloaded in netCDF format and plotted in 10-day bins. Overall, there is some agreement between seismic velocity variations and rainfall variations, especially in the second half of the 2019–2020 PCG5 dataset, but the increase in velocity variation at the end of 2019 begins before the increase in rainfall, thus rainfall is unlikely to be the only driver of the observed variation.

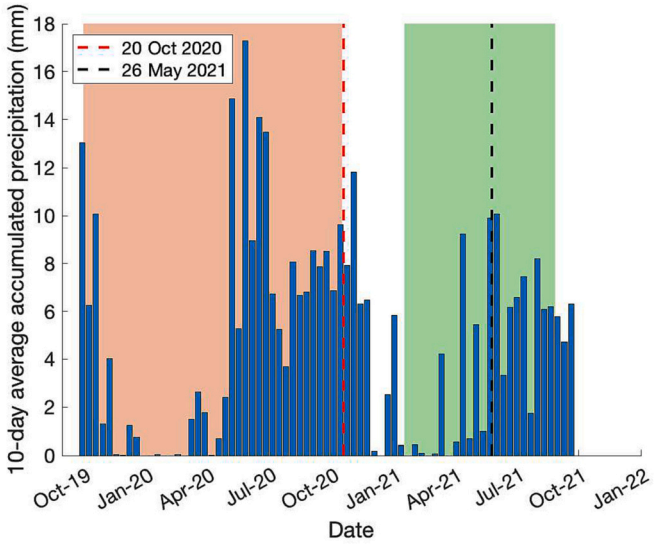

Fig. 16. 10-day average of daily accumulated precipitation over Pacaya obtained from GPM Level 3 IMERG Final Daily 0.1 × 0.1 degree data (blue bars). The red rectangle highlights the overlap with 2019–2020 PCG5 data, and the green rectangle highlights the overlap with 2021 PCG5 data. The vertical red dashed line marks the timing of first vent opening beyond the summit crater on October 10, 2020, and the dashed black line marks the timing of the final ash venting recorded on May 26, 2021. (For interpretation of the references to color in this figure legend, the reader is referred to the web version of this article.)

Overall, the range of variations we observe is comparable to those measured with single-station approaches at Piton de la Fournaise by De Plaen et al. (2016). We note that the 2021 datasets appear much noisier, particularly the SC results, which show several peaks toward the end of the time-series. Given the culmination of the eruption at the end of May, and transition into volcanic quiescence for the rest of the year, it is likely that the sources of noise changed too much during the observation period for coherence to be preserved. Additionally, seismic velocity changes might not be as well delineated due to contamination from continuous tremor signals. Inspection of cross-correlation functions show that at times these are very one-sided and at others more symmetrical, with the one-sidedness suggesting contributions from sources in a particular direction, as opposed to a uniform noise source or well scattered waves (Fig. S42). Finally, both PCG2 and PCG5 lie to the southwest of Pacaya, 3–4 km away from the summit, thereby, we would expect this region to experience fewer changes in the subsurface due to magmatic processes under the edifice and the observed vents. Thus, future seismic assessments at Pacaya would benefit from the availability of data from stations closer to the summit and active vent areas. Nevertheless, we highlight the ease with which these seismic datasets can be computed, and their value even at volcanoes with just one seismometer.

5. Conclusions

We present a geophysical assessment of a heightened eruptive period that took place at Pacaya volcano between October 2020 and May 2021, leveraging access to ground deformation data from 9 SAR datasets acquired by 5 different radar satellite platforms and seismic data from 4 stations. We highlight the advantage of high resolution SAR amplitude imagery for mapping surface changes related to lava flow emplacement, the vulnerability to geometric distortions of low incidence angle platforms, and the challenge of relying on tasking tasking to obtain imagery over volcanoes. Our results underscore the value of access to data from a

variety of platforms with different wavelengths, incidence angles, repeat intervals and spatial resolutions. We emphasize the challenges of coherence loss during periods with widespread lava effusion and ash fall, and the advantages of performing SBAS time-series analysis on shorter subsets of time to retain more pixels in times of lower volcanic activity. Stacking provides a mean to recovering the greatest amount of ground deformation signal as a trade-off with more detailed temporal information. SBAS time-series analysis, on the other hand, enables tracking the evolution of ground deformation with time, while still retaining more coherence than equivalent long interval interferograms. Our time-series results reveal downward and westward displacements on the southwest flank that are compatible with down-dip motion. Given the evidence for previous flank creep at Pacaya during times of similarly vigorous eruptive activity, renewed flank creep is proposed as a likely candidate. However, there may be contributions from lava flow compaction, given the widespread lava effusion, and from known seasonal tropospheric water vapor variations. Based on the available data, RSAM peaks appear to reflect vigor of magma effusion at Pacaya, but a gap in the data impeded the assessment of whether there are recognizable signals in the seismic data that could alert to a change in the behavior of the eruptive activity, such as opening of vents beyond the summit.

CRediT authorship contribution statement

J. Gonzalez-Santana: Conceptualization, Data curation, Formal analysis, Funding acquisition, Investigation, Methodology, Project administration, Validation, Visualization, Writing – original draft. **C. Wauthier:** Conceptualization, Funding acquisition, Methodology, Project administration, Resources, Software, Supervision, Writing – review & editing. **G. Waite:** Formal analysis, Methodology, Supervision, Writing – review & editing.

Declaration of competing interest

The authors declare that they have no known competing financial interests or personal relationships that could have appeared to influence the work reported in this paper.

Data availability

Lava flow and vent shapefiles for: The 2021 eruption of Pacaya Volcano, Guatemala – geophysical analysis through satellite geodesy and seismic noise correlations (Original data) (ScholarSphere). All other data will be made available on request

Acknowledgements

This work was supported by Future Investigators in NASA Earth and Space Science and Technology (FINESST) grant 80NSSC20K1632 and NASA Earth Surface and Interior grant 80NSSC20K0490 issued through the Science Mission Directorate's Earth Science Division. Wauthier also acknowledges support from National Science Foundation CAREER EAR 1945417 grant. TanDEM-X DEM data were provided by DLR (Proposal ID 1552 awarded to C. Wauthier). Sentinel-1 data and precise orbit files were obtained through the ASF Vertex DAAC and from ESA. COSMO-SkyMed data were obtained from ASI through the CEOS Volcano Pilot and Demonstrator working groups. TerraSAR-X data were obtained from DLR through the TerraSAR-X Supersites Download Service and from AIRBUS, as part of the NASA Commercial Smallsat Data Acquisition evaluator. We thank Michael Poland and Julie Griswold for providing the RADARSAT-2 SLC data, courtesy of the National Geospatial Intelligence Agency and the U.S. Geological Survey. ALOS-2 data were obtained from JAXA through G-Portal and the EORC Order Desk (EO-RA3 ALOS-2/4 proposal awarded to C. Wauthier). ASTER data were obtained through the Earth Observing System Data and Information System, through NASA and LPDAAC, and Sentinel-2 and Landsat-8 data were obtained through EarthExplorer and Glovis. We thank Amilcar Roca, Gustavo Chigna, Roberto Merida, and Peter Argueta from INSIVUMEH for useful discussions during the eruptive crisis and a visit to Pacaya in March 2021. We thank Amilcar Roca for access to the seismic data and Lindsey Hernandez for transferring the data. We also thank the editor and the two reviewers, Yosuke Aoki and Lauren Schaefer, for their insightful comments, which helped improve the quality of this manuscript. Computations were performed on The Pennsylvania State University's Institute for Computational and Data Sciences' Roar supercomputer.

Appendix A. Supplementary data

Supplementary data to this article can be found online at https://doi.org/10.1016/j.jvolgeores.2024.108027.

References

Berardino, P., Fornaro, G., Lanari, R., Sansoti, E., 2002. A new algorithm for surface deformation monitoring based on small baseline differential SAR interferograms. IEEE Trans. Geosci. Remote Sens. 40, 2375–2383. URL. https://doi.org/10.1109/TGRS.2002.803792.

Brenguier, F., Shapiro, N.M., Campillo, M., Ferrazzini, V., Duputel, Z., Coutant, O., Nercessian, A., 2008. Towards forecasting volcanic eruptions using seismic noise. Nat. Geosci. 1, 126–130. https://doi.org/10.1038/ngeo104.

Briole, P., Massonnet, D., Delacourt, C., 1997. Post-eruptive deformation associated with the 1986–87 and 1989 lava flows of Etna detected by radar interferometry. Geophys. Res. Lett. 24, 37–40. https://doi.org/10.1029/96GL03705.

Clarke, J., Adam, L., van Wijk, K., 2021. LP or VT signals? How intrinsic attenuation influences volcano seismic signatures constrained by Whakaari volcano parameters. J. Volcanol. Geotherm. Res. 418, 107337. https://doi.org/10.1016/j.jvolgeores.2021.107337.

Cornelius, R.R., Voight, B., 1996. Real-time seismic amplitude measurement (RSAM) and seismic spectral amplitude measurement (SSAM) analyses with the Materials failure Forecast Method (FFM), June 1991 explosive eruption at Mount Pinatubo. In: Fire and Mud: Eruptions and Lahars of Mount Pinatubo, Phillipines. University of Washington Press, Seattle, WA, pp. 249–268. https://pubs.usgs.gov/pinatubo/corn/.

Costantini, M., 1998. A Novel phase Unwrapping Method based on Network programming. IEEE Trans. Geosci. Remote Sens. 36, 813–821. https://doi.org/10.1109/36.673674.

Costantini, M., Rosen, P.A., 1999. A generalized phase unwrapping approach for sparse data, in: IEEE 1999 International Geoscience and Remote Sensing Symposium. IGARSS'99 (Cat. No. 99CH36293). IEEE 267–269. https://doi.org/10.1109/IGARSS.1999.773467.

De Plaen, R.S., Lecocq, T., Caudron, C., Ferrazzini, V., Francis, O., 2016. Single-station monitoring of volcanoes using seismic ambient noise. Geophys. Res. Lett. 43, 8511–8518. https://doi.org/10.1002/2016GL070078.

Donaldson, C., Caudron, C., Green, R.G., Thelen, W.A., White, R.S., 2017. Relative seismic velocity variations correlate with deformation at Klauea volcano. Sci. Adv. 3, e1700219 https://doi.org/10.1126/sciadv.1700219.

Ebmeier, S.K., 2016. Application of independent component analysis to multitemporal InSAR data with volcanic case studies. J. Geophys. Res. Solid Earth 121, 8970–8986. https://doi.org/10.1002/2016JB013765.

Ebmeier, S.K., Biggs, J., Mather, T.A., Amelung, F., 2013. Applicability of InSAR to tropical volcanoes: Insights from Central America. Geol. Soc. Spec. Pub. 380, 15–37. https://doi.org/10.1144/SP380.2.

Endo, E.T., Murray, T., 1991. Real-time Seismic Amplitude Measurement (RSAM): a volcano monitoring and prediction tool. Bull. Volcanol. 53, 533–545. https://doi.org/10.1007/BF00298154.

Global Volcanism Program, 2013. Pacaya (342110) in Volcanoes of the World, v. 4.7.5 Venzke, E (ed.). Smithsonian Institution. https://volcano.si.edu/volcano.cfm?vn=342110.

Goldstein, R.M., Werner, C.L., 1998. Radar interferogram filtering for geophysical applications. Geophys. Res. Lett. 25, 4035–4038. https://doi.org/10.1029/1998GL900033.

Gonzalez-Santana, J., Wauthier, C., 2021. Unraveling long-term volcano flank instability at Pacaya Volcano, Guatemala, using satellite geodesy. J. Volcanol. Geotherm. Res. 410, 107147. https://doi.org/10.1016/j.jvolgeores.2020.107147.

Gonzalez-Santana, J., Wauthier, C., Burns, M., 2022. Links between volcanic activity and flank creep behavior at Pacaya Volcano, Guatemala. Bull. Volcanol. 84, 1–13. https://doi.org/10.1007/s00445-022-01592-2.

Hanssen, R.F., 2001. Radar System Theory and Interferometric Processing. Springer, Netherlands, Dordrecht, pp. 9–60. https://doi.org/10.1007/0–306-47633-9_2.

Huffman, G., Stocker, E., Bolvin, D., Nelkin, E., Tan, J., 2019. GPM IMERG Final Precipitation L3 1 day 0.1 degree x 0.1 degree V06, Edited by Andrey Savtchenko, Greenbelt, MD, Goddard Earth Sciences Data and Information Services Center (GES DISC). Accessed: 12 April 2023. https://doi.org/10.5067/GPM/IMERGDF/DAY/06.

Kitamura, S., Matías, O., 1995. Tephra Stratigraphic Approach to the Eruptive History of Pacaya Volcano, Guatemala. Science Reports of the Tohoku University, 7th Series (Geography), vol. 45, pp. 1–41.

Krischer, L., Megies, T., Barsch, R., Beyreuther, M., Lecocq, T., Caudron, C., Wassermann, J., 2015. ObsPy: a bridge for seismology into the scientific Python ecosystem. Computational Science & Discovery 8, 014003. https://doi.org/10.1088/1749-4699/8/1/014003.

Lecocq, T., Caudron, C., Brenguier, F., 2014. MSNoise, a python package for monitoring seismic velocity changes using ambient seismic noise. Seismol. Res. Lett. 85, 715–726. https://doi.org/10.1785/0220130073.

Liu, Z., Liang, C., Zhu, Z., Wang, L., Jiang, N., Wang, C., Wu, Z., 2019. The complex velocity variation induced by the precipitation and the 2018 eruption of the Kilauea Volcano in Hawaii revealed by ambient noise. Seismol. Res. Lett. 90, 2154–2164. https://doi.org/10.1785/0220190053.

Lundgren, P., Usai, S., Sansosti, E., Lanari, R., Tesauro, M., Fornaro, G., Berardino, P., 2001. Modeling surface deformation observed with synthetic aperture radar interferometry at Campi Flegrei caldera. Journal of Geophysical Research: Solid Earth 106, 19355–19366. https://doi.org/10.1029/2001jb000194.

Massonnet, D., Feigl, K.L., 1998. Radar interferometry and its application to changes in the Earth's surface. Rev. Geophys. 36, 441–500. https://doi.org/10.1029/97RG03139 arXiv:arXiv:1011.1669v3.

Matías Gomez, R.O., Rose, W.I., Palma, J.L., Escobar-Wolf, R., 2012. Notes on a Map of the 1961–2010 Eruptions of Volcán de Pacaya, Guatemala. The Geological Society of America Digital Map and Chart Series, 10. https://doi.org/10.1130/2012.DMCH010.

Naismith, A.K., Watson, I.M., Escobar-Wolf, R., Chigna, G., Thomas, H., Coppola, D., Chun, C., 2019. Eruption frequency patterns through time for the current (1999–2018) activity cycle at Volcán de Fuego derived from remote sensing data: evidence for an accelerating cycle of explosive paroxysms and potential implications of eruptive activity. J. Volcanol. Geotherm. Res. 371, 206–219. https://doi.org/10.1016/j.jvolgeores.2019.01.001.

Pinel, V., Poland, M.P., Hooper, A., 2014. Volcanology: Lessons learned from Synthetic Aperture Radar imagery. J. Volcanol. Geotherm. Res. 289, 81–113. https://doi.org/10.1016/j.jvolgeores.2014.10.010.

Power, J.A., Murray, T.L., Marso, J.N., Laguerta, E.P., Newhall, C., Punongbayan, R., 1996. Preliminary observations of seismicity at Mount Pinatubo by use of the seismic spectral amplitude measurement (SSAM) system, May 13–June 18, 1991. In: Fire and Mud: Eruptions and Lahars of Mount Pinatubo, Philippines, Philippine Institute of Volcanology and Seismology, Quezon City, and University of Washington Press, Seattle, pp. 269–283. https://pubs.usgs.gov/pinatubo/power/.

Rose, W.I., Palma, J.L., Wolf, R.E., Matías Gomez, R.O., 2013. A 50 yr eruption of a basaltic composite cone: Pacaya, Guatemala. The. Geol. Soc. Am. Spec. Pap. 498, 1–21. https://doi.org/10.1130/2013.2498(01).

Samsonov, S.V., 2019. User manual, source code, and test set for MSBASv3 (Multidimensional Small Baseline Subset version 3) for one-and two-dimensional deformation analysis. Geomatics Canada. https://doi.org/10.4095/313749.

Samsonov, S., D'Oreye, N., 2012. Multidimensional time-series analysis of ground deformation from multiple InSAR data sets applied to Virunga Volcanic Province. Geophys. J. Int. 191, 1095–1108. https://doi.org/10.1111/j.1365-246X.2012.05669.x.

Samsonov, S.V., D'Oreye, N., 2017. Multidimensional small baseline subset (MSBAS) for two-dimensional deformation analysis: Case study Mexico City. Can. J. Remote. Sens. 43, 318–329. https://doi.org/10.1080/07038992.2017.1344926.

Schaefer, L., Lu, Z., Oommen, T., 2015. Dramatic volcanic instability revealed by InSAR. Geology 43, 743–746. https://doi.org/10.1130/G36678.1.

Schaefer, L.N., Wang, T., Escobar-Wolf, R., Oommen, T., Lu, Z., Kim, J., Lundgren, P.R., Waite, G.P., 2017. Three-dimensional displacements of a large volcano flank movement during the May 2010 eruptions at Pacaya Volcano, Guatemala. Geophys. Res. Lett. 44, 135–142. https://doi.org/10.1002/2016GL071402.

Siebert, L., Alvarado, G.E., Valance, J.W., van Wyk de Vries, B., 2006. Large-volume volcanic edifice failures in Central America and associated hazards. In: Volcanic hazards in Central America: Geological Society of America Special Paper 412 v, 1–26. https://doi.org/10.1130/2006.2412(01.

Simons, M., Rosen, P.A., 2015. Interferometric Synthetic Aperture Radar Geodesy. In: Treatise on Geophysics, , 2 ed.vol. 3. Elsevier, Amsterdam, pp. 339–385. https://doi.org/10.1016/B978-0-444-53802-4.00061-0. chapter 3.

Stephens, C.D., Chouet, B.A., Page, R.A., Lahr, J.C., Power, J.A., 1994. Seismological aspects of the 1989–1990 eruptions at Redoubt Volcano, Alaska: the SSAM perspective. Journal of Volcanology and Geothermal Research 62, 153–182. https://doi.org/10.1016/0377-0273(94)90032-9.

Tárraga, M., Carniel, R., Ortiz, R., Marrero, J., Garca, A., 2006. On the predictability of volcano-tectonic events by low frequency seismic noise analysis at Teide-Pico Viejo volcanic complex, Canary Islands. Nat. Hazards Earth Syst. Sci. 6, 365–376. https://doi.org/10.5194/nhess-6-365-2006.

Vallance, J.W., Siebert, L., Rose, W.I., Girón, J.R., Banks, N.G., 1995. Edifice collapse and related hazards in Guatemala. J. Volcanol. Geotherm. Res. 66, 337–355. https://doi.org/10.1016/0377-0273(94)00076-S.

Werner, C., Wegmuller, U., Strozzi, T., Wiesmann, A., 2001. GAMMA SAR and Interferometric Processing Software. Proceedings of the ERS-Envisat Symposium, Gothenburg.

Wnuk, K., Wauthier, C., 2017. Surface deformation induced by magmatic processes at Pacaya Volcano, Guatemala revealed by InSAR. J. Volcanol. Geotherm. Res. 344, 197–211. URL: doi: https://doi.org/10.1016/j.jvolgeores.2017.06.024.